

1 **Impact of scale-aware deep convection on the cloud liquid and ice water paths and precipitation using the**  
2 **Model for Prediction Across Scales (MPAS-v5.2)**

3 **Laura D. Fowler<sup>1</sup>, Mary C. Barth<sup>1</sup>, and Kiran Alapaty<sup>2</sup>**

4 <sup>1</sup>National Center for Atmospheric Research, Boulder, Colorado

5 <sup>2</sup>Center for Environmental Measurements and Modeling, U.S. Environmental Protection Agency  
6 Research Triangle Park, North Carolina

7  
8  
9 Revised for Geoscientific Model Development

10 February 2020  
11  
12  
13  
14  
15  
16  
17  
18  
19  
20  
21  
22  
23  
24  
25  
26  
27  
28  
29  
30  
31  
32  
33  
34  
35  
36  
37  
38  
39  
40  
41  
42  
43  
44  
45  
46  
47  
48

49 *Corresponding author address:* Dr. Laura D. Fowler, National Center for Atmospheric Research. P.O. Box 3000,  
50 Boulder, CO 80307-3000, USA.

51 E-mail: [laura@ucar.edu](mailto:laura@ucar.edu)

52        **Abstract.** The cloud Liquid Water Path (LWP), Ice Water Path (IWP), and precipitation simulated with uniform-  
53 and variable-resolution numerical experiments using the Model for Prediction Across Scales (MPAS) are compared  
54 against Clouds and the Earth’s Radiant Energy System (CERES) and Tropical Rainfall Measuring Mission data. Our  
55 comparison between monthly mean model diagnostics and satellite data focuses on the convective activity regions of  
56 the Tropical Pacific Ocean, extending from the Eastern Tropical Pacific Basin where trade wind boundary layer clouds  
57 develop to the Western Pacific warm pool defined by deep convective updrafts capped with extended upper-  
58 tropospheric ice clouds. Using the scale-aware Grell-Freitas (GF) and Multi-Scale Kain-Fritsch (MSKF) convection  
59 schemes in conjunction with the Thompson cloud microphysics, uniform-resolution experiments produce large biases  
60 between simulated and satellite-retrieved LWP, IWP, and precipitation. Differences in the treatment of shallow  
61 convection lead the LWP to be strongly overestimated when using GF while being in relatively good agreement when  
62 using MSKF compared to CERES data. Over areas of deep convection, uniform- and variable-resolution experiments  
63 overestimate the IWP with both MSKF and GF, leading to strong biases in the top-of-the-atmosphere long- and short-  
64 wave radiation relative to satellite-retrieved data. Mesh refinement over the Western Pacific warm pool does not lead  
65 to significant improvement in the LWP, IWP, and precipitation due to increased grid-scale condensation and upward  
66 vertical motions. Results underscore the importance of evaluating clouds, their optical properties, and the top-of-the-  
67 atmosphere radiation budget in addition to precipitation when performing mesh refinement global simulations.

## 68    **1    Introduction**

69    Comparing simulated against observed global cloud liquid and ice water paths (LWP and IWP) remains challenging  
70 because of uncertainties in parameterizing moist processes and cloudiness in global climate and numerical weather  
71 prediction (NWP) models, and errors in retrieving the LWP and IWP from satellite measurements. Cloud simulations  
72 from general circulation models (GCMs) involved in Phase 3 and 5 of the Coupled Model Intercomparison Project  
73 (CMIP3; CMIP5; Meehl et al, 2007; Taylor et al., 2012) display a strong disparity in the simulated LWP (Jiang et al.,  
74 2012; Li et al., 2018) and IWP (Li et al., 2012), producing annual mean LWP and IWP overestimated by factors of 2  
75 to 10 compared to satellite data. Satellite observations of the LWP and IWP from passive nadir viewing instruments  
76 such as the Moderate-resolution Imaging Spectroradiometer (MODIS; Minnis et al., 2011), and profiling radar such  
77 as the 94-GHz instrument on the CloudSat satellite (Stephens et al., 2002), also display major differences among  
78 themselves, as discussed in Li et al. (2008) and Waliser et al. (2009). While models and satellite retrievals agree that  
79 the LWP and IWP should be defined as the vertically-integrated liquid and ice water content, including all  
80 nonprecipitating and precipitating hydrometeors, this is not always the case in practice, further challenging a clearly-  
81 posed data-data and model-data comparison. Defining the LWP and IWP varies between models, depending on the  
82 complexity of the parameterization of cloud microphysics processes and prognostic versus diagnostic treatment of  
83 falling hydrometeors. Defining the measured LWP and IWP varies between satellite products, depending on the  
84 sensitivity of the observing systems to detect large precipitating particles. While comparing simulated and observed  
85 LWP and IWP may not be as straightforward as comparing the top-of-the-atmosphere (TOA) radiation budget (Dolinar  
86 et al., 2015; Stanfield et al., 2015), it offers a different way to directly diagnose biases in simulated total cloud liquid

87 and ice water mass as a first step to help correct deficiencies in parameterizing global scale moist processes and  
88 precipitation.

89 Before the launch of the CloudSat and Cloud-Aerosol Lidar and Infrared Pathfinder Satellite Observation mission  
90 (Stephens et al., 2002), global estimates of the LWP and IWP were retrieved principally from satellite radiance  
91 measurements over different spectral intervals (e.g., Alishouse et al., 1990; Greenwald et al., 1993; Minnis et al., 1995;  
92 Platnick et al., 2003). In their critical review of most common methods developed to retrieve cloud and precipitation  
93 properties from satellite radiances, Stephens and Kummerow (2007) identify two main sources of errors. The first  
94 source of errors originates from the mandatory classification between cloudy and cloud-free scenes, and between  
95 precipitating and non-precipitating cloudy scenes. The second source of errors stems from using forward radiative  
96 transfer models that lack details of the vertical distribution of cloudiness and precipitation as well as complexity in  
97 specifying the optical properties of liquid water and ice particles. Estimating the LWP and IWP from CloudSat radar  
98 reflectivities alone presents its own set of challenges for scenes that include precipitating cloud systems due to the  
99 high sensitivity of radar reflectivities to the presence of large particles, for scenes that include mixed-phase and deep  
100 convective clouds, and close to the surface due to ground clutter. Li et al. (2018) show that annual mean maps of  
101 MODIS- and CloudSat-based LWP agree relatively well in tropical and subtropical regions if both data sets exclude  
102 LWP observations for deep convective/precipitating clouds since MODIS is quite insensitive to precipitation.  
103 Stephens and Kummerow (2007) advocate combining satellite-retrieved radar and radiance measurements to help  
104 validate simulated cloud properties and precipitation. In addition to considering the impact of precipitating particles,  
105 Waliser et al. (2009) demonstrate that a well-posed model-data comparison must include a consistent sampling  
106 between model outputs and satellite data to reduce diurnal sampling biases and sensitivity of the sensor and retrieval  
107 algorithm to the particle size when computing the simulated LWP and IWP.

108 Contemporary climate and NWP GCMs (Giorgetta et al., 2018; Molod et al., 2012; Kay et al., 2015, Skamarock  
109 et al., 2012) categorize moist processes into three distinct parameterizations, one to simulate turbulent mixing in the  
110 Planetary Boundary Layer (PBL) in response to surface forcing and forcing in the free troposphere, one to simulate  
111 subgrid scale shallow and deep convection, and one to include grid-scale cloud microphysics. While coupling between  
112 parameterizations varies between GCMs, it is an established practice to let detrained condensates from convective  
113 updrafts serve as sources for non-convective grid-scale clouds, as precipitating anvils and cirrus outflow. We suggest  
114 that uncertainties in parameterizing moist convection and impact on grid-scale clouds may explain a major part of the  
115 differences in the LWP and IWP simulated between the CMIP3 and CMIP5 GCMs. In recent years, efforts have been  
116 made to develop unified cloud parameterizations to represent all cloud types and alleviate the need to parameterize  
117 complex interactions between stratiform, shallow convective, and deep convective clouds (Guo et al., 2015; Storer et  
118 al., 2015; Thayer et al., 2015). Using the global Model for Prediction Across Scales (MPAS; Skamarock et al., 2012),  
119 Fowler et al. (2016) discuss the sensitivity of simulated precipitation as spatial resolution increases from hydrostatic  
120 to nonhydrostatic scales, and suggest to further analyze the associated sensitivity of simulated clouds and TOA  
121 radiation. Results show that as subgrid scale convective motions are increasingly resolved, diagnostic precipitation  
122 from the scale-aware Grell-Freitas (GF; Grell and Freitas, 2014) deep convection scheme decreases while prognostic  
123 precipitation from the WSM6 (Hong and Lim, 2006) cloud microphysics scheme increases over the refined area of

124 the variable-resolution mesh. Vertical profiles of the cloud liquid and ice water mixing ratios and cloud fraction  
125 highlight the redistribution of cloud condensates and relative humidity with height in the refined area in response to  
126 decreased contribution of convective detrainment of cloud liquid water and ice. However, Fowler et al. (2016) do not  
127 further address if variations in the vertical profiles of cloud condensates lead to improved LWP, IWP, and cloud optical  
128 properties against satellite-derived data.

129 The objectives of our research are threefold. First, we want to assert that our suite of PBL, deep and shallow  
130 convection, and cloud microphysics parameterizations tested in MPAS at hydrostatic and nonhydrostatic scales for  
131 medium-range spring forecasts over the Continental United States (Schwartz, 2019; Wong and Skamarock, 2016) can  
132 also be used to produce month-long simulations of tropical convection, narrowing our analysis on the Tropical Pacific  
133 Ocean. In order to broaden our research and possibly generalize our results, we also implemented the scale-aware  
134 MultiScale Kain-Fritsch (MSKF; Glotfelty et al., 2019; Zheng et al., 2016) parameterization of deep and shallow  
135 convection in addition to GF. Second, we want to evaluate the ability of MPAS to simulate the LWP, IWP, cloudiness,  
136 and TOA long- and short-wave radiation against the Clouds and the Earth’s Radiant Energy System (CERES; Wielicki  
137 et al., 1996) Single Scanner FootPrint (SSF; Minnis et al., 2011) data set, and precipitation against the TRMM  
138 Multisatellite Precipitation Analysis (TMPA; Huffman et al., 2007). Our third goal aims at understanding differences  
139 in the LWP, IWP, precipitation, and cloud radiative effects as functions of horizontal resolution with GF and MSKF  
140 using the capability of local mesh refinement developed for MPAS.

141 In Section 2, we summarize the characteristics of the GF and MSKF parameterizations of deep and shallow  
142 convection. In Section 3, we provide a short description of MPAS, including physics parameterizations used with both  
143 convective parameterizations, the design of our experiments using the uniform- and variable-resolution meshes, and  
144 description of the satellite data sets used to validate our results. In Section 4, we analyze our results in terms of  
145 precipitation and varying contribution of the convective and grid-scale precipitation to the total precipitation as a  
146 function of horizontal resolution. In Section 5, we compare the LWP, IWP, and TOA long- and short-wave radiation  
147 against satellite data. In Section 6, we summarize our results and propose areas of future research.

## 148 **2 Description of the convective parameterizations**

149 Mass flux-based convective parameterizations distinguish themselves through the use of different triggering  
150 functions to initiate convection, the details of their entraining-detraining cloud models, and formulation of their  
151 closures that control the intensity of convection and computation of the cloud base mass flux. For convective  
152 parameterizations that include deep and shallow convection, criteria that characterize the two kinds of convection  
153 strongly vary. Furthermore, how convective parameterizations account for the dependence of convection on the  
154 horizontal resolution differs in complexity. In this section, we summarize the chief characteristics of GF and MSKF,  
155 including differences in their treatment of deep and shallow convection, and spatial-scale dependence.

### 156 **2.1 The Grell-Freitas (GF) parameterization**

157 The version of GF used in our numerical experiments is that implemented in version 3.8.1 of the Advanced  
158 Research Weather Research Forecast model (Skamarock et al., 2008), as described in Grell and Freitas (2014). Its

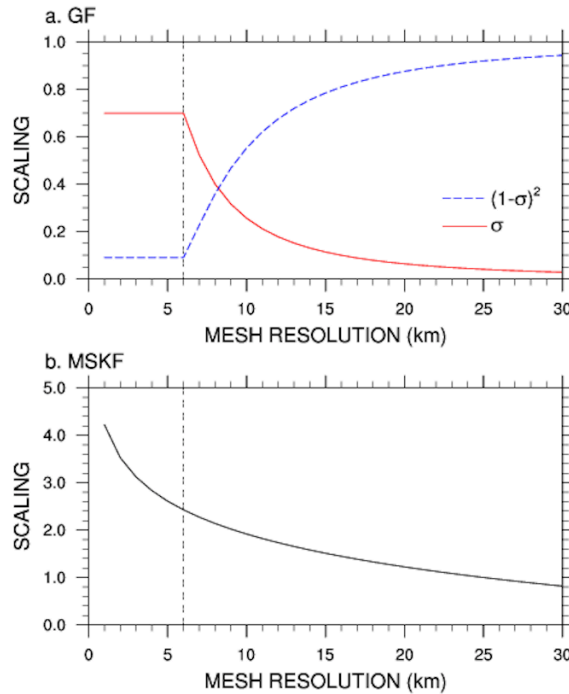
159 properties were first discussed in Grell (1993) and later expanded by Grell and Devenyi (2002) to include  
 160 stochasticism. GF treats deep and shallow convection separately by using different initial entrainment rates ( $7 \times 10^{-5}$   
 161  $\text{m}^{-1}$  and  $1 \times 10^{-2} \text{m}^{-1}$  for deep and shallow convection, respectively) to control the depth of convective cloud layers and  
 162 closures to calculate the cloud base mass flux. GF includes an ensemble of closures from well-known convective  
 163 parameterizations to compute a mean cloud-base mass flux. For deep convection, these four closures are the *AS* closure  
 164 (Arakawa and Schubert, 1974) that assumes instantaneous equilibrium between the large-scale forcing and subgrid-  
 165 scale convection; the *W* closure (Brown, 1979; Frank and Cohen, 1987) that relates the cloud base mass flux to the  
 166 grid-scale upward vertical velocity; the *MC* closure (Krishnamurti et al., 1983) that calculates the cloud base mass  
 167 flux as a function of the vertically-integrated vertical moisture advection; and the *KF* closure (Kain and Fritsch, 1993)  
 168 that reduces the convective available potential energy over a prescribed convective time-scale. Qiao and Liang (2015)  
 169 analyze the separate and combined impacts of the four closures on the simulated summer precipitation over the United  
 170 States coastal oceans. On the one hand, they found that computing the cloud base mass flux using the *W* and *MC*  
 171 closures led to precipitation patterns and amounts that are in better agreement against TMPA data than those using the  
 172 *AS* and *KF* closures. On the other hand, they found that the *AS* and *KF* closures yield improved diurnal cycle of  
 173 precipitation relative to the other two closures. In our numerical experiments, GF gives an equal weight to each closure  
 174 to calculate the mean cloud base mass flux for deep convection. As for deep convection, GF includes different closures  
 175 for shallow convection. In our numerical experiments using GF, we choose the boundary layer quasi-equilibrium  
 176 (*BLQE*) closure of Raymond (1995) for shallow convection.

177 Both types of convection transport total water and moist static energy in a conservative manner but neglect to  
 178 include ice phase processes in updrafts and downdrafts. In this version of GF, the only feedback between shallow  
 179 convection and the large-scale environment is lateral and cloud-top detrainment of water vapor and corresponding  
 180 heating, as liquid water formed in shallow updrafts evaporates immediately. Deep convection returns potential  
 181 temperature, water vapor, and condensed water tendencies to the environment. Detrained condensed water acts as a  
 182 source of liquid water (ice) if the large-scale temperature is warmer (colder) than the prescribed 258 K threshold.  
 183 While GF assumes that shallow convective plumes are not deep enough to produce precipitation, the conversion of  
 184 liquid water to rain water in deep convective plumes depends on a simple Kessler-type (Kessler, 1969) conversion  
 185 threshold and precipitation reaches the surface instantaneously.

186 As discussed in Grell and Freitas (2014), deep convection includes a simplified representation of the unified  
 187 parameterization of deep convection described in Arakawa and Wu (2013). Arakawa and Wu (2013) demonstrate that  
 188 mass flux-based convective parameterizations can be modified to work at all resolutions spanning between hydrostatic  
 189 and nonhydrostatic scales through the reduction of the convective vertical eddy transport as a quadratic function of  
 190 the horizontal fraction of the grid box occupied by convective updrafts. In GF, the convective updraft fraction ( $\sigma$ ) is  
 191 computed as a simple function of the initial entrainment rate ( $\varepsilon = 7 \times 10^{-5} \text{m}^{-1}$ ) and half-width radius ( $R$ ) of convective  
 192 updrafts following Simpson and Wiggert (1969), or

$$\sigma = \frac{\pi R^2}{A} \quad \text{and} \quad R = \frac{0.2}{\varepsilon} \tag{1}$$

194 where  $A$  is the area of the grid box. In Eq. (1),  $\sigma$  is not allowed to exceed 0.7. As discussed in Fowler et al. (2016),  
 195 when  $\sigma$  becomes greater than 0.7,  $\sigma$  is set to 0.7 and  $\varepsilon$  is recalculated using Eq. (1), leading to increased entrainment  
 196 and decreased convective cloud-tops as  $A$  becomes smaller. Another option would be to turn off deep convection when  
 197  $\sigma$  reaches values close to 1, in which case a better choice for its maximum value may be between 0.9 and 1 (Grell and  
 198 Freitas, 2014). Figure 1.a highlights the rapid decrease in  $\sigma$  from 0.7 to 0.3 as spatial resolution decreases from 6 to  
 199 9 km.  $\sigma$  further decreases from 0.3 to 0.1 for resolutions between 9 and 16 km, and from 0.1 to 0.05 for resolutions  
 200 between 16 and 30 km. The  $(1-\sigma)^2$  quadratic function used to scale the mass flux starts to be significant at resolutions  
 201 greater than 20 km and decreases rapidly to a minimum value of 0.1 for horizontal grid-spacing smaller than 6 km.  
 202 Using a maximum value for  $\sigma$  ensures that over the most refined area of the mesh, parameterized deep convection is  
 203 not completely turned off since deep convection is not explicitly resolved. Using a variable-resolution mesh varying  
 204 between 50 km over the coarse area of the mesh down to 3 km over the refined area of the mesh centered over South  
 205 America, Fowler et al. (2016) show that the impact of parameterized deep convection weakens and that of grid-scale  
 206 cloud microphysics strengthens as horizontal grid-spacing increases from hydrostatic to nonhydrostatic scales.



207 **Figure 1:** a) Convective updraft fraction as a function of the mesh resolution used to scale the cloud base mass flux in GF; and b)  
 208 Scaling factor as a function of the mesh resolution used to scale the convective time scale in MSKF.  
 209

## 2.2 The Multi-Scale Kain-Fritsch (MSKF) parameterization

211 MSKF is the scale-aware version of the Kain-Fritsch (KF) convective parameterization, first developed by Kain  
 212 and Fritsch (1990; 1993), and later updated by Kain (2004) to include, among other improvements, non-precipitating  
 213 shallow convection. The trigger function is that used in Fritsch and Chappell (1980), originally tested in Kain and  
 214 Fritsch (1992) and recently in Suhas and Zhang (2014). In MSKF, convection may be triggered if the temperature of  
 215 a *mixed layer* is greater than that of the environment. The pressure thickness of that mixed layer must be at least 50

216 hPa thick and is computed as the sum of adjacent layer depths starting at the layer next to the surface. The mixed layer  
 217 temperature is a pressure-weighted function of the temperatures in those adjacent layers after being lifted to the Lifting  
 218 Condensation Level (LCL) plus a perturbation temperature linked to the magnitude of the grid-scale vertical motion  
 219 at the LCL. Once the base of a potential updraft source layer is found, convection remains activated if the vertical  
 220 velocity of an air parcel lifted using the Lagrangian parcel method remains positive for a minimum cloud depth of 3  
 221 km, as a test that the convective instability is strong enough for the air parcel to reach the Level of Free Convection  
 222 (LFC). If not, the procedure is repeated by moving up to the next model layer until a new updraft source layer is found  
 223 or until the search reaches above the lowest 300 hPa of the atmosphere. Further details on the equations used to  
 224 compute the perturbation temperature and parcel vertical velocity are found in Kain (2004).

225 In MSKF, the closure assumption assumes that the Convective Available Potential Energy in a cloud layer is  
 226 removed within a time adjustment period following Bechtold et al. (2001). The convective time scale is defined as the  
 227 advective time scale in the cloud layer with maximum values of 1 h and 0.5 h for deep and shallow convection,  
 228 respectively. In contrast to GF, the thermodynamics inside the cloud model includes the ice phase. The condensed  
 229 water formed in each cloudy layer is partitioned between liquid water and ice, assuming a linear transition of the cloud  
 230 temperature between 268 K and 248 K. A fraction of the condensed water converts to rain, following Ogura and Cho  
 231 (1973), and reaches the ground instantaneously. As discussed in Kain (2004), when an updraft source layer is  
 232 identified, the classification of a convective cloud layer as deep or shallow depends on the cloud depth. Shallow  
 233 convection is activated when all the criteria for deep convection are met, but the depth of the updraft is shallower than  
 234 the minimum cloud depth (3 km). This definition implies that shallow and deep convection are not allowed to coexist.  
 235 In the case of shallow convection, precipitation formed in updrafts is detrained to the environment as rain or snow,  
 236 providing an additional moisture source to the large-scale environment. As in GF, MSKF provides tendencies of  
 237 temperature, water vapor, cloud liquid water/ice to the environment, and tendencies of rain and snow from shallow  
 238 convection.

239 MSKF contains many improvements over KF, as summarized in the supplemental material of Glotfelty et al.  
 240 (2019). These improvements include subgrid-scale cloud feedbacks to radiation from both shallow and deep  
 241 convection leading to more realistic surface downward radiation, as described in Alapaty et al. (2012), and the scale  
 242 dependence of fundamental parameters so that MSKF can be used at spatial resolutions varying between hydrostatic  
 243 and nonhydrostatic scales. As detailed in Glotfelty et al. (2019) and Zheng et al. (2016), MSKF uses a scale dependent  
 244 formulation ( $\beta$ ) to the adjustment time scale ( $\tau$ ) for deep and shallow convection based on Bechtold et al. (2008), or

$$245 \quad \tau = \frac{H}{W_{cl}} \beta \quad \text{and} \quad \beta = 1 + \ln\left(\frac{25}{\Delta x}\right) \quad (2)$$

246 where  $H$  and  $W_{cl}$  are the depth of the convective cloud and cloud-averaged vertical velocity scale, and  $\Delta x$  is the grid  
 247 spacing. Figure 1.b highlights the dependence of the  $\beta$  scaling parameter as a function of horizontal resolution. As  
 248 many MSKF parameters are optimized for a resolution around 25 km (Kain, 2004),  $\beta$  is equal to 1 at 25 km, ramping  
 249 up to values greater than 2.4 for resolutions higher than 6km. Because the adjustment time scale is proportional to  
 250  $\beta$  (Zheng et al., 2016), it increases as horizontal resolution increases, leading to scale-aware stabilization of the  
 251 atmosphere by MSKF. In addition, MSKF includes a new scale-aware formulation of the minimum entrainment rate

252 using the LCL as a function of the scale-dependent *Tokioka* parameter (Tokioka et al., 1988), a scale-dependent  
253 conversion rate for liquid water and ice condensates to precipitation, an increased grid-scale velocity expressed in  
254 terms of the subgrid scale updraft mass flux, and elimination of double counting of precipitation in cloudy layers. The  
255 separate and combined impacts of the development of MSKF on high resolution weather forecasts and regional climate  
256 simulations are discussed in Herwehe et al. (2014), Mahoney (2016), He and Alapaty (2018), Zheng et al. (2016), and  
257 Glotfelty et al. (2019).

## 258 **3 Methodology**

### 259 **3.1 Numerical experiments**

260 We discuss differences in our MPAS results between GF and MSKF configurations on precipitation, cloud  
261 properties, and TOA radiation using 30-day long numerical experiments in MPAS (Skamarock et al., 2012). MPAS  
262 is a global nonhydrostatic atmospheric model developed for NWP and climate studies. The horizontal discretization  
263 uses an unstructured spherical centroidal Voronoi tessellation with a C-grid staggering, as described in Ju et al. (2011),  
264 while the vertical discretization is the height-based hybrid terrain-following coordinate of Klemp (2011). The  
265 dynamical solver integrates the prognostic equations (cast in flux form) for the horizontal momentum, vertical  
266 velocity, potential temperature, dry air density, and scalars using the split-explicit technique of Klemp et al. (2007).  
267 The temporal discretization uses a third-order Runge-Kutta scheme and the explicit time-splitting technique described  
268 in Wicker and Skamarock (2002). We use the monotonic option of the scalar transport scheme of Skamarock and  
269 Gassmann (2011) for horizontal and vertical advection of all moist scalars on the unstructured Voronoi mesh. Finally,  
270 horizontal filtering of the state variables is based on Smagorinsky (1963), as described in Skamarock et al. (2012). For  
271 variable-resolution meshes, the eddy viscosity coefficient is scaled as a function of the inverse mesh density so that  
272 horizontal diffusion is increased in the coarse area relative to the refined area of the mesh.

273 In MPAS, the computational flow includes three distinct steps. The first step calls the physics parameterizations  
274 that update the surface energy budget and calculate the tendencies of potential temperature, moist species, and zonal  
275 and meridional wind due to long- and short-wave radiation, sub-grid scale convection, condensation and mixing in  
276 the PBL and free troposphere, and gravity wave drag due to orography. The physics parameterizations use the same  
277 input surface boundary conditions and soundings to compute their respective tendencies. Besides GF and MSKF, these  
278 parameterizations are,

- 279 • the Noah land surface parameterization described by Chen and Dudhia (2001),
- 280 • the long- and short-wave Rapid Radiative Transfer Model for GCMs (RRTMG) described by Mlawer et al. (1997)  
281 and Iacono et al. (2000),
- 282 • the semi-empirical parameterization of the cloud fraction of grid-scale clouds from Xu and Randall (1996) and  
283 convective clouds from Xu and Krueger (1991) for use in the long- and short-wave RRTMG schemes. Following  
284 Xu and Randall (1996), the fractional amount of grid-scale clouds is a function of the relative humidity and grid-  
285 averaged condensate mixing ratio of cloud liquid water, ice, and snow. In MSKF, the fractional amount of shallow  
286 and deep convective clouds depends on the convective mass flux.



- 287 • the Mellor–Yamada–Nakanishi–Niino (MYNN) Planetary Boundary Layer (PBL) and surface layer scheme  
288 described by Nakanishi and Niino (2009) with many updates described in Olson et al. (2019), and
- 289 • the gravity wave-drag parameterization of Hong et al. (2008).

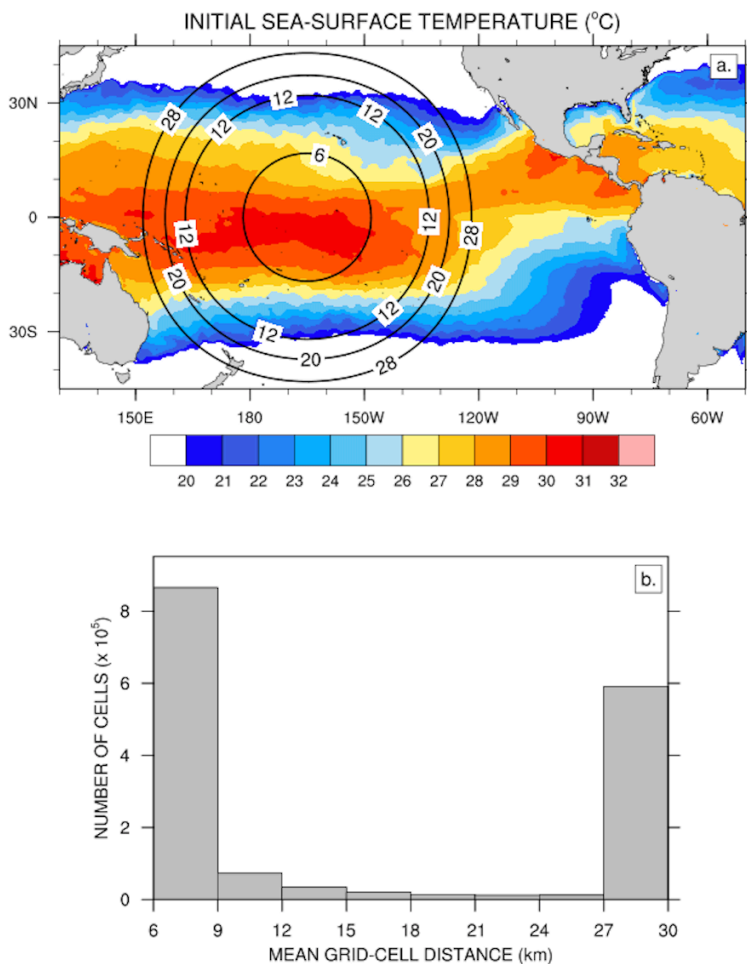
290 The second step calls the dynamical solver which updates the state variables with their respective diabatic  
291 tendencies in conjunction to applying horizontal and vertical advection. Finally, the third step calls the grid-scale cloud  
292 microphysics parameterization so that at the end of the model time step, supersaturation has been entirely removed or  
293 the relative humidity does not exceed 100%. Unlike the physics parameterizations listed for step one, the grid-scale  
294 cloud microphysics scheme updates the potential temperature and moist species for the next time step instead of  
295 providing individual tendencies. The bulk cloud microphysics parameterization of Thompson et al. (THOM; 2004,  
296 2008) is used in all our numerical experiments. THOM includes prognostic equations for temperature, mass mixing  
297 ratio of water vapor, cloud liquid water, rain, cloud ice, snow, and graupel, and number concentration of cloud ice and  
298 rain. We set the number concentration of cloud droplets to  $300 \times 10^6 \text{ m}^{-3}$  over land and  $100 \times 10^6 \text{ m}^{-3}$  over oceans. In  
299 RRTMG, we diagnose the radiative effective radii of cloud liquid water, cloud ice, and snow as functions of the  
300 THOM cloud particle assumptions to add coupling between the cloud microphysics and cloud optical properties, as  
301 discussed in Thompson et al. (2016).

302 To compare the two convective parameterizations against satellite-derived data at hydrostatic scales, we use a  
303 quasi-uniform resolution mesh for which the mean distance between cell centers is 30 km, corresponding to 655,362  
304 cells. The vertical scale includes 55 layers with monotonically increasing thicknesses varying from 50 meters next to  
305 the surface to 700 meters below 10 km to 1000 meters below the model top over ocean cells. The model top is set at  
306 30 km. The dynamics and physics time steps are both set to 150 s, and the horizontal diffusion length scale is set to  
307 30 km. Long- and short-wave radiation is called every 15 mins and THOM is cycled twice so that the cloud  
308 microphysics time-step is less than 90 s to ensure computational stability (Thompson, private communication). With  
309 each convection scheme, we have performed a one-month long experiment preceded by a two-day spin-up to simulate  
310 Northern Hemisphere early winter, initializing our experiments with ERA-Interim (Dee et al., 2011) reanalyses for  
311 0000 UTC 29 November 2015. ERA-Interim sea surface temperatures and sea ice fractions are used to update ocean  
312 cells daily. We refer to our quasi-uniform resolution experiments run with GF and MSKF as GFu and MSKFu,  
313 respectively.

### 314 **3.2 Sensitivity experiments**

315 Using a variable-resolution mesh spanning between 50 km and 3 km in MPAS, Fowler et al. (2016) demonstrate  
316 that subgrid-scale convection parameterized with GF weakens and grid-scale cloud microphysics parameterized with  
317 WSM6 (Hong and Lim, 2006) strengthens as resolution increases from the coarse to most refined area of the mesh.  
318 Over the most refined area, grid-scale precipitation contributes a major part to total precipitation, and vertical profiles  
319 of subgrid-scale convective heating and drying resemble those obtained with a precipitating shallow convection  
320 scheme. Fowler et al. (2016) suggest investigating the effect of variable resolution on cloud macrophysical properties  
321 and TOA radiation, as grid-scale cloud microphysics parameterizations provide a more physically-based description  
322 of condensation and precipitation over the refined area of the mesh, compared to simpler entraining-detraining cloud

323 models used in parameterized convection schemes. With the aim to quantify changes in cloud properties and radiation  
 324 across scales using GF and MSKF, we repeat the early winter experiments but with a variable-resolution mesh that  
 325 spans between 30 km and 6 km and includes 1,622,018 cells. As shown in Fig. 2.a, we centered the refined area of the  
 326 mesh over the Pacific warm pool which we defined as the area in the Western Pacific Ocean where sea-surface  
 327 temperatures (SSTs) exceed 28.5°C, or between 170°E and 140°W. East of 140°W, the north-south width of warmest  
 328 SSTs across the transition zone between the refined and coarse mesh narrows to delineate the location of the ITCZ in  
 329 the Tropical Eastern Pacific. West of 170°E, the end of mesh refinement borders the eastern tip of Papua New Guinea.  
 330 Along the Equator, the transition zone between nonhydrostatic and hydrostatic scales spans 20° in the meridional  
 331 direction on either side of the most refined area of the mesh. Figure 2.b displays a histogram of the mean



332 **Figure 2:** a) Initial sea-surface temperature and refined variable-resolution mesh depicted using isolines of the mean distance  
 333 between grid-cell centers (km) over the Tropical Pacific Ocean; and b) histogram of the number of cells as a function of the mean  
 334 distance between grid-cell centers.  
 335

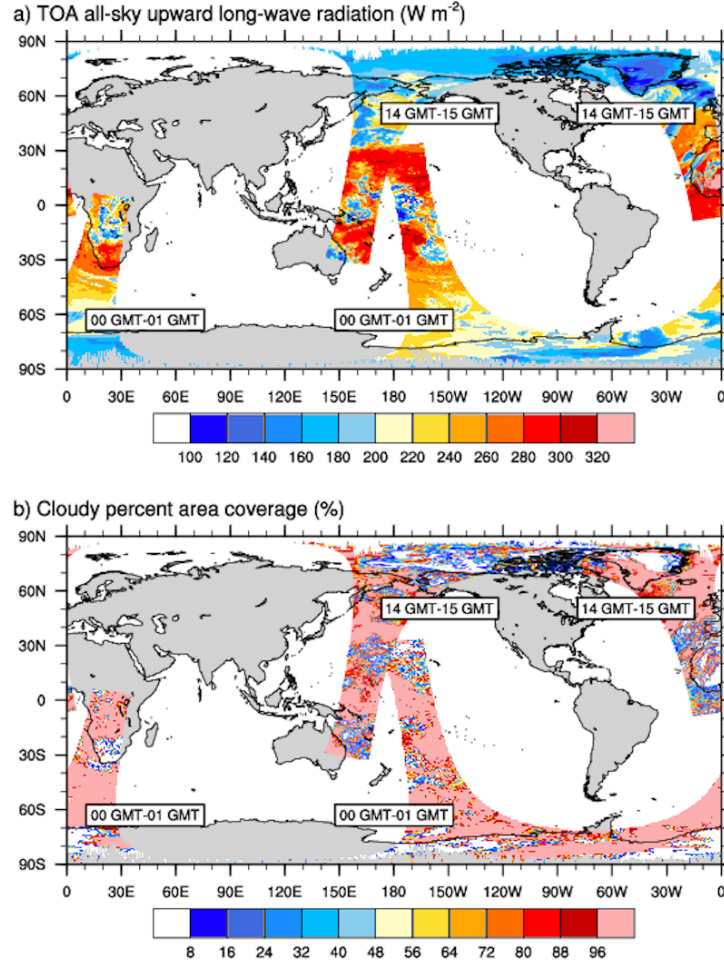
336 distance between cell centers. Differences between the initialization of the variable- versus quasi uniform-  
 337 resolution experiments include a reduced time-step from 150 s to 30 s and a reduced horizontal diffusion length scale  
 338 from 30 km to 6 km. Also, THOM is called only once per time-step. We refer to our variable-resolution experiments  
 339 run with GF and MSKF as GFv and MSKFv, respectively. Differences between GFu, GFv, MSKFu, and MSKFv are  
 340 listed in Table 1.

	GFu	MSKFu	GFv	MSKFv
No. of cells	655,362	655,362	1,622,018	1,622,018
Min. cell distance (km)	22.8	22.8	4.4	4.4
Max. cell distance (km)	31.8	31.8	37.8	37.8
Time step (s)	150	150	30	30
Minimum diffusion length scale (km)	30	30	6	6
CP	GF	MSKF	GF	MSKF

342 **Table 1:** Horizontal mesh resolution, minimum and maximum distance between grid-cell centers, time-step, horizontal diffusion  
343 length scale, and convective parameterization (CP) for numerical experiments with the quasi uniform- and variable-resolution  
344 meshes.

### 345 3.3 Satellite data sets

346 We compare the cloud liquid water path (LWP) and ice water path (IWP), cloud area fraction (CF), and the top-  
347 of-the-atmosphere longwave upward (TOALW) and shortwave net (TOASW) radiation simulated in our numerical  
348 experiments against the Edition-4 Single Scanner Footprint (SSF) products from the Clouds and the Earth’s Radiant  
349 Energy System (CERES; Wielicki et al., 1996). Minnis et al. (2011) describe in great details the retrieval of  
350 simultaneous and collocated radiation fluxes and cloud properties from the CERES radiometers and the Moderate-  
351 resolution Imaging Spectroradiometer (MODIS) using consistent algorithms and calibration across satellite platforms,  
352 and shared auxiliary input (temperature and humidity profiles). SSF data are available in two different formats. The  
353 first data file format contains one hour of radiation fluxes and cloud properties at the instantaneous CERES 20 km  
354 footprint level from the sun-synchronous afternoon (morning) equatorial crossing time Aqua (Terra) satellites. As  
355 illustrated in Minnis et al. (2011; their Fig. 15), the CF in each SSF is given in terms of a clear fraction, a fraction for  
356 an upper and lower cloud layer separately, and a fraction for an upper layer over a lower layer, although the overlap  
357 CF is not available and set to zero in the Edition 4 release version that we are using. The LWP, IWP, and all other  
358 cloud fields are provided for the lower and upper layers, separately. Figure 3 illustrates two orbits of the Aqua satellite,  
359 one between 00 GMT and 01 GMT, and one between 14 GMT and 15 GMT, showing the TOALW (top panel) and  
360 CF (bottom panel), after gridding the hourly orbital data to a  $0.2^\circ \times 0.2^\circ$  latitude-longitude grid. Gridded radiation fluxes  
361 and cloud data are means over all SSF data contained inside each rectangular grid, after applying a linear interpolation  
362 to reduce the number of missing values. Missing values, highlighted in gray in all figures, depict rectangular grids that  
363 did not contain radiation and cloud data in any of the SSF inside the  $0.2^\circ \times 0.2^\circ$  grid. As seen in Fig. 3, our gridding of  
364 the orbital data removes most of the missing data along each orbit, providing a clear depiction of the relationship  
365 between the TOALW and CF for cloudy and cloud-free grid cells. Areas of high (low) TOALW coincide with areas  
366 of small (large) cloudy areas, but it is also interesting to note that areas of each orbit are characterized as overcast in  
367 conjunction with areas that are not as spatially uniform in TOALW as in CF.

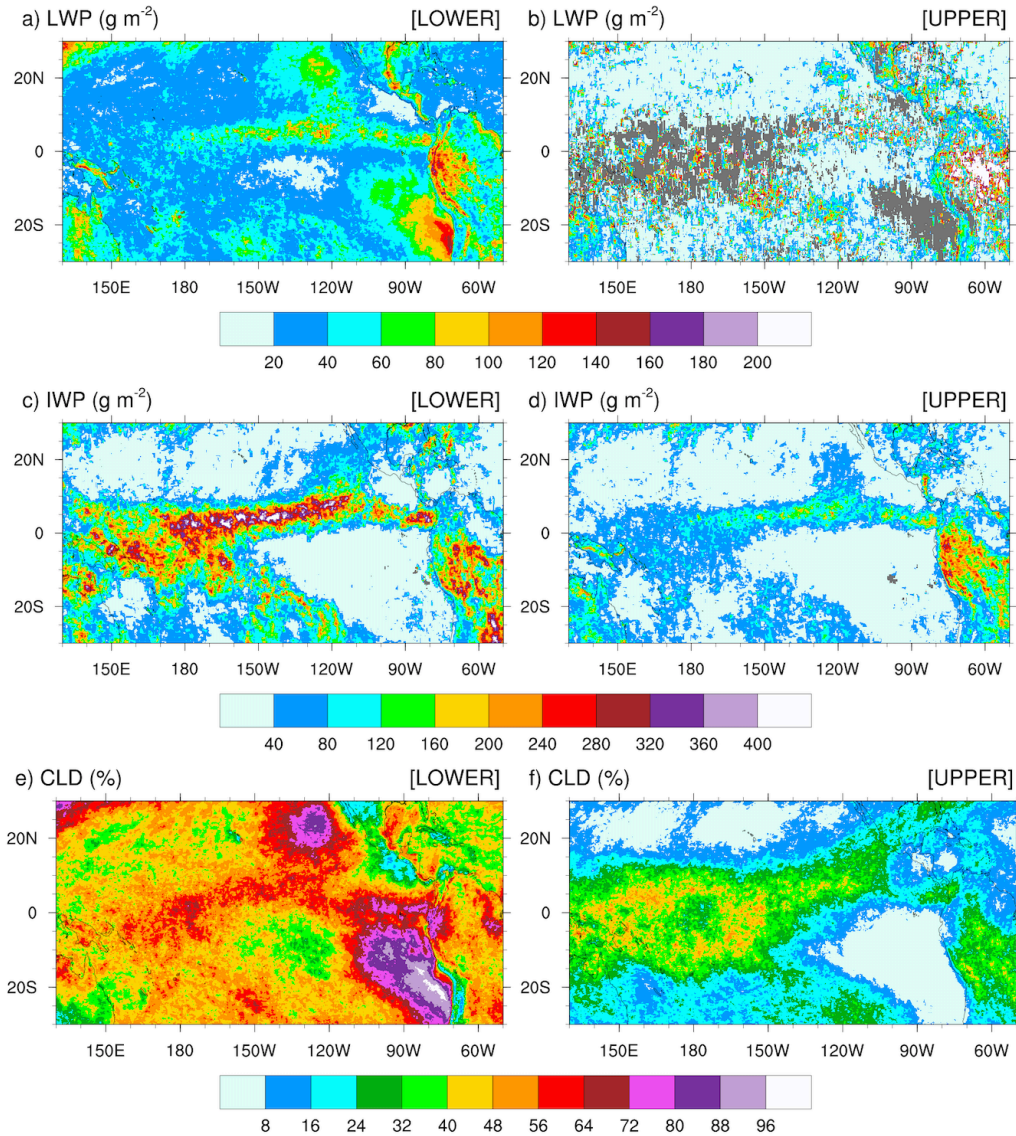


368  
 369 **Figure 3:** Orbital paths of the Aqua satellite between 00 GMT-01 GMT and 14 GMT-15 GMT after binning the SSF data onto a  
 370  $0.2^{\circ} \times 0.2^{\circ}$  rectangular grid for a) the TOA all-sky upward long-wave radiation, and b) the cloudy percent area coverage for 1<sup>st</sup>  
 371 December 2015.

372 The second data file format (SSF1deg) includes daily and monthly averages of the original SSF orbital data but  
 373 interpolated on a  $1^{\circ} \times 1^{\circ}$  latitude-longitude grid. The difficulty in using hourly higher-resolution orbital data instead of  
 374 monthly mean lower-resolution  $1^{\circ} \times 1^{\circ}$  latitude-longitude gridded product is that the former are available in two distinct  
 375 *dynamic* layers while the latter is provided at fixed pressure levels and for the atmospheric column. The lower and  
 376 upper layers are referred to as *dynamic* layers because the cloud-top (base) pressure of each layer varies between SSFs  
 377 along each orbit. The advantage of using orbital hourly data is that they can be gridded and interpolated to a spatial  
 378 resolution close to that of our uniform and variable-resolution numerical experiments prior to computing monthly  
 379 mean radiation and cloud fields. We choose the  $0.2^{\circ} \times 0.2^{\circ}$  latitude-longitude gridded hourly data derived from the first  
 380 data file format through the entire manuscript.

381 In order to best compare the simulated against satellite-derived LWP and IWP, we need to understand the  
 382 partitioning of the SSF LWP and IWP between the two cloud layers. In brief, a lower and an upper cloud layer can be  
 383 detected simultaneously if they lie adjacent to each other inside an SSF. In that case, the cloud properties for each  
 384 layer are reported separately. In the case when an opaque upper cloud layer is detected to be above a lower cloud  
 385 layer, it is impossible to identify the two layers separately. Then, only one cloud layer is reported and always classified

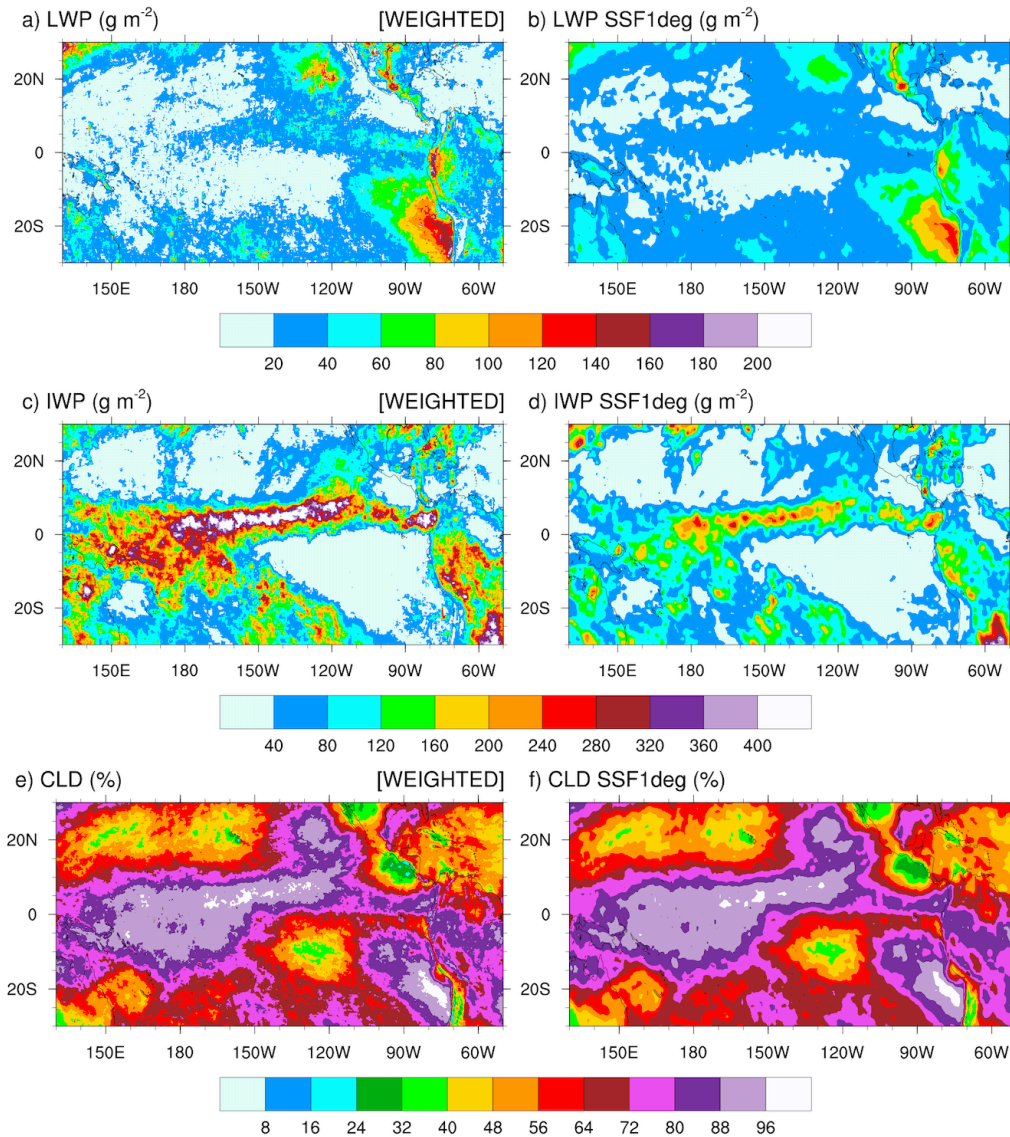
386 as the lower cloud layer, regardless of its cloud-base (top) pressure (Loeb, private communication). Further details on  
387 the cloud classification, including determination of the cloud phase, are found in Geier et al. (2003) and Minnis et al.  
388 (2011). Figure 4 shows the monthly-mean LWP, IWP, and CF for the lower (left panels) and upper (right panels) layer  
389 measured by Aqua for December 2015 over the Tropical Pacific Ocean. Figure S1 is as Fig. 4, but for the Terra satellite  
390 (see supplemental figures). LWP and IWP are *in-cloud* values meaning that they have not been weighted by CF. The  
391 lower cloud layer includes stratiform clouds that form over colder sea-surface temperatures along the coast of Peru  
392 and off the Baja Peninsula. Over these areas of CF greater than 72% for the lower cloudy layer, CF for the upper cloud  
393 layer is less than 8%, highlighting that a single layer of low-level clouds fills a major fraction of the SSF. Increased  
394 values of CF are seen in conjunction with increased (decreased) values for the LWP (IWP) in the lower cloud layer  
395 indicative of warm-phase clouds, as well seen as off the coast of Peru. High values for the CF and IWP juxtaposed  
396 with lower values for the LWP in the lower cloud layer depict clearly deep convection over the Eastern Pacific Ocean,  
397 ITCZ, and warm pool region. Over areas of deep convection, upper cloud layers are often detected in conjunction with  
398 lower cloud layers within the same SSF but are defined by decreased values for the CF and IWP. For the LWP, the  
399 coexistence of a lower and upper cloud layer is quite infrequent, as seen by the number of missing grid-points in Fig.  
400 4.b (S1.b). Where detected, the LWP in the upper layer exceeds that in the lower layer, indicative of warm-phase  
401 mature thicker cumulus clouds coexisting with developing thinner cumulus clouds in the lower layer. Finally, outside  
402 of the typical stratus cloud regions and either sides of the ITCZ and warm pool region, SSF data reveal extended  
403 regions of warm-phase thinner clouds characteristic of widespread shallow convection over tropical oceans.



404  
 405 **Figure 4:** Monthly-mean cloud liquid water path (LWP, top panels), cloud ice water path (IWP, middle panels), and cloud fraction  
 406 (CLD, bottom panels) over the Tropical Pacific Ocean for December 2015 from the Aqua satellite. Panels a), c), and e) are for the  
 407 lower cloud layer; panels b), d), and f) are for the upper cloud layer.

408 Calculating the satellite-retrieved LWP and IWP in an atmospheric column for validation of those from our  
 409 numerical simulations is a two-step process. Because simulated LWPs and IWPs are *gridcell mean* values and not  
 410 *local* values, we first multiply the SSF LWP and IWP by CF to get their mean values in the lower and upper cloud  
 411 layers separately, prior to gridding the hourly orbital data. Second, because the lower and upper layers are defined as  
 412 adjacent to each other and never overlap in a SSF, we simply add the gridcell mean LWP and IWP in the lower layer  
 413 to that in the upper layer to compute the total LWP and IWP. Our processing method is simpler than the processing  
 414 steps taken by the CERES Science Team to spatially grid and temporally average SSF hourly orbital data to SSF1deg  
 415 gridded monthly mean data. Figure 5 compares the monthly-mean  $0.2^\circ \times 0.2^\circ$  latitude-longitude CF-weighted LWP  
 416 and IWP and CF (left panels) against the SSF1deg products (right panels) for December 2015 over the Tropical Pacific  
 417 Ocean. The top panels of Fig. 5 show that our method reproduces successfully the geographical patterns and magnitude

418 of the LWP over the Tropical Pacific when compared against the SSF1deg data for both months. In contrast, because  
 419 our method does not weigh the IWP as a function of height, it systematically overestimates the SSF IWP when  
 420 compared against the SSF1deg data, as seen over the ITCZ and South Pacific Convergence Zone (SPCZ) in both  
 421 months.  
 422



423 **Figure 5:** Monthly-mean cloudy area-weighted cloud liquid water path (LWP, top panels), cloudy-area weighted cloud ice water  
 424 path (IWP, middle panels), and cloud fraction (CLD, bottom panels) over the Tropical Pacific Ocean for December 2015. Panels  
 425 a), c), and e) are SSF data; panels b), d), and f) are SSF1deg climatological data.  
 426

427 Using ice water content data from the ascending (daytime) and descending (nighttime) portion of CloudSat orbits,  
 428 Waliser et al. (2009; Fig. 7) estimate that day-night fluctuations in the ice water content at 215 hPa account for as  
 429 much as 13% (20 %) of the annual mean ice water content over the warm pool (Tropical Eastern Pacific), in response  
 430 to the diurnal cycle of deep convection over the tropical oceans. Therefore, when computing the monthly-mean CF,  
 431 LWP, IWP, TOALW, and TOASW produced with GFu, GFv, MSKFu and MSKFv, we first sample the hourly model

432 diagnostics in accordance with the Aqua and Terra satellite orbits in order to reduce biases from different diurnal  
433 sampling between our experiments and SSF data. Because the MODIS-based retrieval of the LWP and IWP is  
434 insensitive to precipitation, and the rain, snow, and graupel mixing ratios are prognostic variables in THOM and fall  
435 through the atmosphere at finite velocities, we infer that the LWP and IWP must include all precipitating and non-  
436 precipitating condensates.

437 In addition to CERES SSF data, we use the monthly-mean precipitation rates from the TRMM Multisatellite  
438 Precipitation Analysis (TMPA Version 7; Huffman et al., 2007) to compare simulated versus observed precipitation  
439 rates, and monthly mean ERA-Interim reanalyses (Dee et al., 2011) to compare simulated versus observed precipitable  
440 water in the lower troposphere.

## 441 **4 Simulated versus satellite-retrieved precipitation**

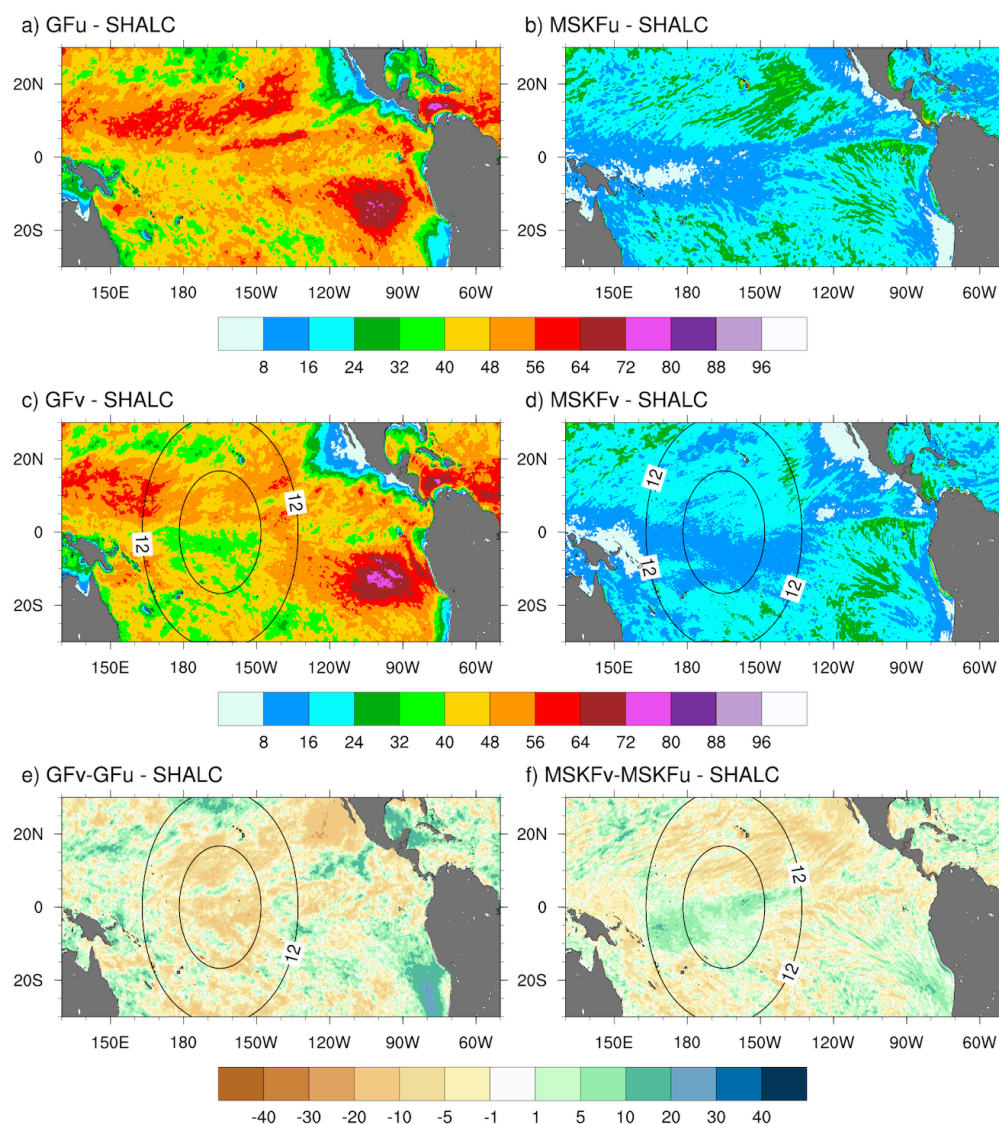
### 442 **4.1 Incidence of subgrid-scale shallow and deep convection**

443 Differences in the treatment of interactions between shallow and deep convection in GF and MSKF, as described  
444 in Section 2, are bound to modify the partitioning between shallow and deep convection as spatial resolution increases  
445 over the refined area of the mesh. A useful diagnostic to analyze the response of shallow and deep convection to local  
446 mesh refinement is the incidence of convection. Because shallow convection in both GF and MSKF is non-  
447 precipitating, we set the incidence of shallow convection to 100 % when cloud-tops of shallow convective updrafts  
448 are detected, and 0 % otherwise. We set the incidence of deep convection to 100 % when convective precipitation  
449 occurs and 0 % otherwise. Figures 6 and 7 highlight the impact of the horizontal scale dependence of convection on  
450 the monthly-mean incidence of subgrid-scale shallow and deep convection in our uniform- and variable-resolution  
451 experiments for December 2015.

452 Figure 6 shows that simulated shallow convection occurs over the entire Tropical Pacific, and that its incidence  
453 is about twice as large in GFu and GFv as in MSKFu and MSKFv. In GFu and GFv, incidence in excess of 48 %  
454 covers most of the Tropical Pacific, including the ITCZ and warm pool where GF allows shallow and deep convection  
455 to occur simultaneously. GFu and GFv exhibit highest incidence of shallow convection off the coast of Peru where  
456 persistent low-level stratiform clouds are formed. In contrast, the incidence of shallow convection in MSKFu and  
457 MSKFv never exceeds 32 % over the entire domain and is less than 16 % over the ITCZ and warm pool where shallow  
458 and deep convection are not allowed to coexist in MSKF. The bottom panels highlight differences in the incidence of  
459 shallow convection between GFv and GFu, and MSKFv and MSKFu. Despite the fact that GF does not include a  
460 spatial scale dependence in its formulation of shallow convection, GFv produces reduced shallow convection relative  
461 to GFu over most of the Tropical Pacific, except most notably immediately off the coast of Peru. In contrast to GFv,  
462 MSKFv yields increased incidence of shallow convection over most of the warm pool region. In MSKF, the height of  
463 deep convective clouds decreases as horizontal resolution increases. As the classification between deep and shallow  
464 convection is a function of cloud depth, convective clouds originally defined as deep are reclassified as shallow,  
465 leading to increased incidence of shallow convection in the refined area of the mesh.



INCIDENCE OF SHALLOW CONVECTION (%)



466  
 467 **Figure 6:** Monthly-mean incidence of shallow convection (SHALC) over the Tropical Pacific Ocean simulated in GFu and MSKFu  
 468 (top panels) and GFv and MSKFv (middle panels), and difference in the incidence of shallow convection between GFv and GFu  
 469 (bottom left panel) and MSKFv and MSKFu (bottom right panel) for December 2015.

470 In Fig. 7, the top and middle panels show that, in contrast to shallow convection, the incidence of deep convection  
 471 has the same order of magnitude in GFu and MSKFu, and GFv and MSKFv. The top panels reveal that the incidence  
 472 of deep convection is higher in MSKFu than GFu over the ITCZ and warm pool. In MSKFu, a sharp transition between  
 473 areas of high and low incidence of deep convection causes areas outside of the ITCZ and warm pool to be mostly void  
 474 of deep convection, as seen between 10°N and 30°N. In GFu, the incidence of deep convection is decreased over the  
 475 warm pool relative to the ITCZ west of 160°W. Outside of the ITCZ and warm pool, GFu and GFv lead to higher  
 476 incidence of deep convection than MSKFu and MSKFv because, in contrast to MSKF, GF allows deep and shallow  
 477 convection to coexist in the same grid-cell. Middle panels highlight decreased incidence of subgrid-scale deep  
 478 convection inside the refined area of the mesh over the warm pool in both GFv and MSKFv, as we expect clouds to

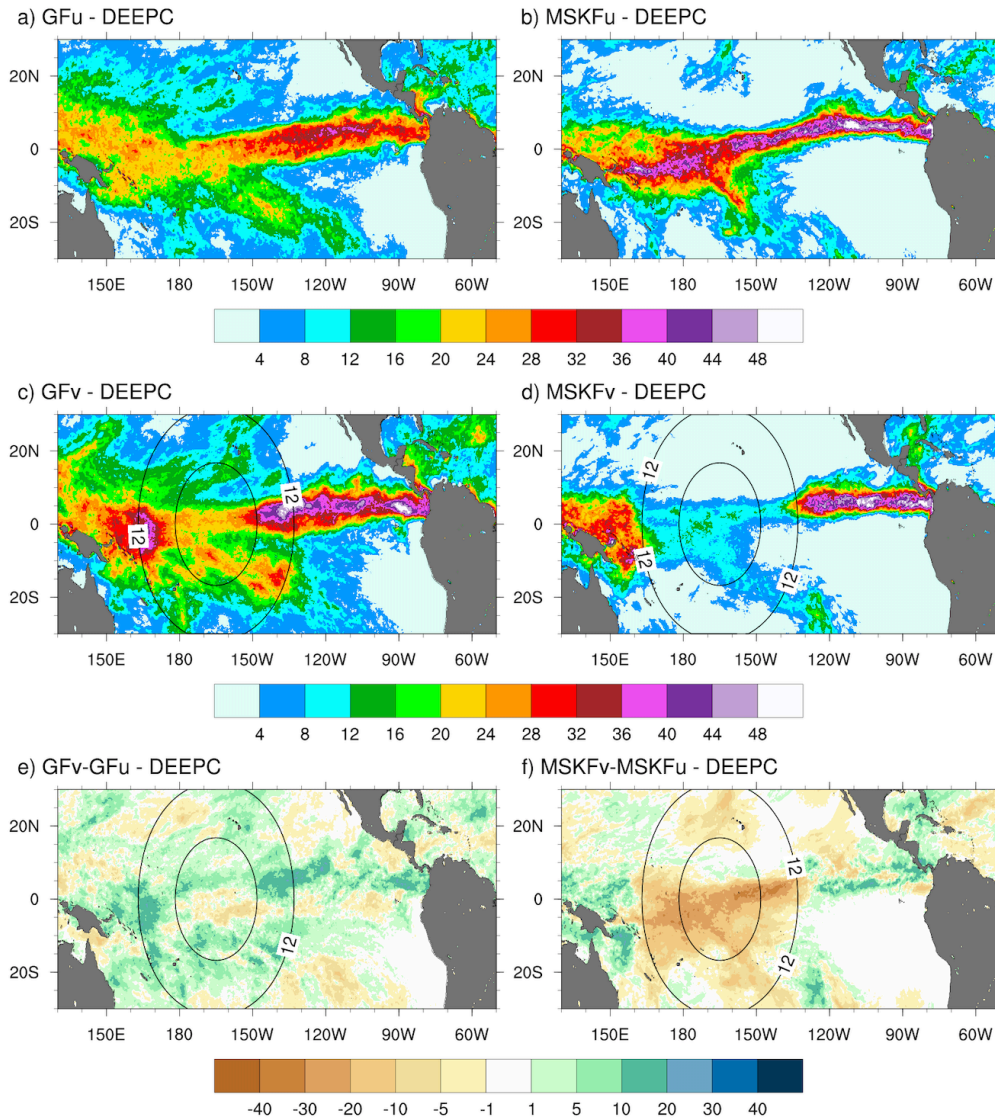
479 be resolved on the higher resolution grid, in conjunction with increased incidence east and west of the refined area.  
 480 The decreased incidence in the refined area is more pronounced between MSKFu and MSKFv than between GFu and  
 481 GFv whereas the upscaling impact of spatial refinement outside the refined area is greater in GFv than MSKFv. The  
 482 scale-aware formulation in GF does not produce the same contrast between the refined and coarse mesh in GFv and  
 483 GFu as that in MSKF in MSKFv and MSKFu. Fig. 7.f reveals a reduced incidence in excess of 25 % between MSKFu  
 484 and MSKFv starting at resolutions higher than 12 km flanked by increased incidence of deep convection east and west  
 485 of the refined area. In contrast, Fig. 7.e displays a longitudinal band of decreased incidence of deep convection between  
 486 90°W and the dateline, bordered by increased deep convection north of the equator and south of 10°S. Table 2 lists  
 487 the area-averaged incidence of deep and shallow convection for an area inside the refined mesh (REFINED: 0.1°N to  
 488 5.1°N; 150°W to 180°W) and an area over the Tropical Eastern Pacific (EAST: 3.1°N to 8.1°N; 90°W to 120°W), as  
 489 later shown in Figure 9.a. The REFINED and EAST areas display little variation in the incidence of shallow  
 490 convection between GFu (MSKFu) and GFv (MSKFv), but the incidence of shallow convection in GFu and GFv is  
 491 much higher than in MSKFu and MSKFv. The incidence of subgrid-scale deep convection is higher in the EAST area  
 492 compared to the REFINED area in all four experiments. Over the REFINED area, the incidence of subgrid-scale deep  
 493 convection remains about the same between GFu and GFv but strongly decreases between MSKFu and MSKFv.  
 494

	DEEP CONVECTION (%)		SHALLOW CONVECTION (%)	
	REFINED	EAST	REFINED	EAST
GFu	20	30	52	52
GFv	23	36	47	48
MSKFu	27	33	14	17
MSKFv	10	36	17	15

495 **Table 2:** Area-averaged incidence of deep and shallow convection. The REFINED and EAST areas are shown in Figure 9.a.

496 As described in Section 2, MSKF differentiates shallow from deep convection as a function of the convective  
 497 cloud depth. As spatial resolution increases, the scale aware formulation leads to a reduction in the intensity of  
 498 convection and depth of convective clouds, mostly deep convection, over the refined area as seen in Fig. 7.f. As the  
 499 depth of convective clouds originally classified as precipitating deep convective clouds become shallower, MSKF  
 500 reclassifies those same clouds as nonprecipitating shallow clouds, leading to near-equal compensation between the  
 501 decreased and increased incidence of deep and shallow convection over the warm pool. In contrast to MSKF, GF  
 502 causes precipitating deep convection to become precipitating shallow convection at increased spatial resolution. As  
 503 this process occurs in the deep convection scheme and both cloud types precipitate, variations in the incidence of deep  
 504 convection between GFu and GFv are small. Further analysis of the response of shallow convection between GFu and  
 505 GFv over the refined area is beyond the objectives of this research.

INCIDENCE OF DEEP CONVECTION (%)

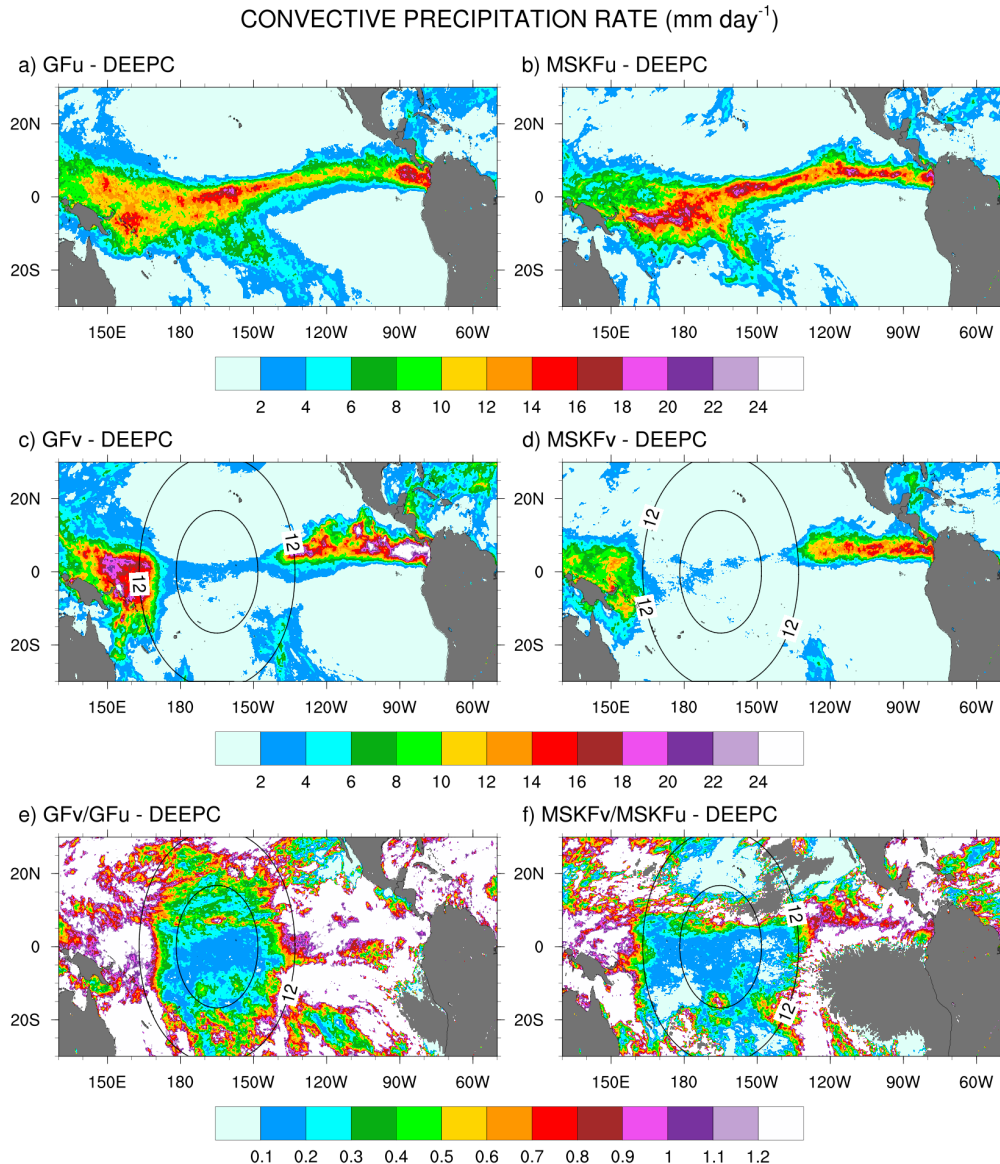


506  
507 **Figure 7:** As Fig. 6, but for the monthly-mean incidence of deep convection (DEEPC).

508 **4.2 Precipitation rates**

509 Figure 8 shows the monthly-mean convective precipitation rate simulated in GFu and MSKFu (top panels), and  
 510 GFv and MSKFv (middle panels). The bottom panels in Figure 8 display the ratio between the convective precipitation  
 511 rate simulated in GFv (MSKFv) and GFu (MSKFu) to contrast the impact of the scale aware formulation in GF and  
 512 MSKF. The top panels highlight similar geographical patterns of convective precipitation in GFu and MSKFu.  
 513 Between 80°W and 160°W, increased convective precipitation is located along the ITCZ, in conjunction with  
 514 increased incidence of deep convection, as seen in Figs. 7.a-b. West of 160°W, GFu leads to decreased but more  
 515 widespread convective precipitation relative to MSKFu over the warm pool, in conjunction with decreased but more  
 516 widespread incidence of convection. In GF, this result infers that while deep convection is not triggered as often over  
 517 the warm pool as along the ITCZ, the amount of convective precipitation produced in one time-step is higher over the

518 warm pool than along the ITCZ, so that monthly-mean convective precipitation rates remain about the same in both  
519 regions. In Fig. 8, and in agreement with the middle panels of Fig. 7, middle panels display a strong decrease in  
520 convective precipitation in both GFv and MSKFv over the refined area of the mesh. In MSKFv, the strong reduction  
521 in convective precipitation occurs, not only over the most refined area of the mesh, but also where horizontal grid-  
522 spacing increases from 6 to 12 km. Convective precipitation increases sharply as soon as grid-spacing is greater than  
523 12 km. In GFv, the monthly-mean convective precipitation rate is higher than that in MSKFv over the most refined  
524 area of the mesh but starts to increase more rapidly between 6 and 12 km than in MSKFv. Differences in increasing  
525 convective precipitation across the transition zone between the refined and coarse areas reflect different impacts of  
526 the scale-aware formulation in GF and MSKF. In order to start understanding the strong increase in convective  
527 precipitation across the transition zones in GFv, we run GFu with the 30s time step used in GFv to quantify the  
528 dependence of a shorter time-step on a coarser resolution mesh with GF. As seen in Fig. S2.a, reducing the time step  
529 from 150s to 30s yields increased convective precipitation over all the convectively active areas of the Tropical Pacific  
530 Ocean. Differences in convective precipitation (Fig. S2.b) display maxima over the Tropical Eastern Pacific (east of  
531 110°W) and east of Papua New Guinea (east of 160°E), and superimpose relatively well with maxima display in GFv  
532 east and west of the refined area of the mesh seen in Fig. 8.c. This result implies that some of the closures used in GF  
533 are sensitive to the model time step. Further research is needed to investigate how the troposphere in GFv becomes  
534 more unstable than MSKFv between the refined and coarse area of the mesh. The bottom panels in Figure 8 show that  
535 the ratio in convective precipitation between GFv and GFu has the same order of magnitude as that between MSKFv  
536 and MSKFu over the refined area of the mesh. While it remains as small in the transition zone as in the refined mesh  
537 with MSKF, this ratio increases to values greater than 1 between 6 and 12 km with GF, indicating increased convective  
538 precipitation on each side of the refined area in GFv relative to GFu, as also seen in Figure 8.c. Maps of monthly-  
539 mean grid-scale precipitation rate would show similar geographical patterns of grid-scale precipitation between GFu  
540 and MSKFu. Over the refined area, increased grid-scale precipitation compensates decreased convective precipitation  
541 in GFv and MSKFv. Over the coarse area, grid-scale precipitation is strongly decreased along the ITCZ and warm  
542 pool in GFv while remaining nearly the same in MSKFv (not shown for brevity).

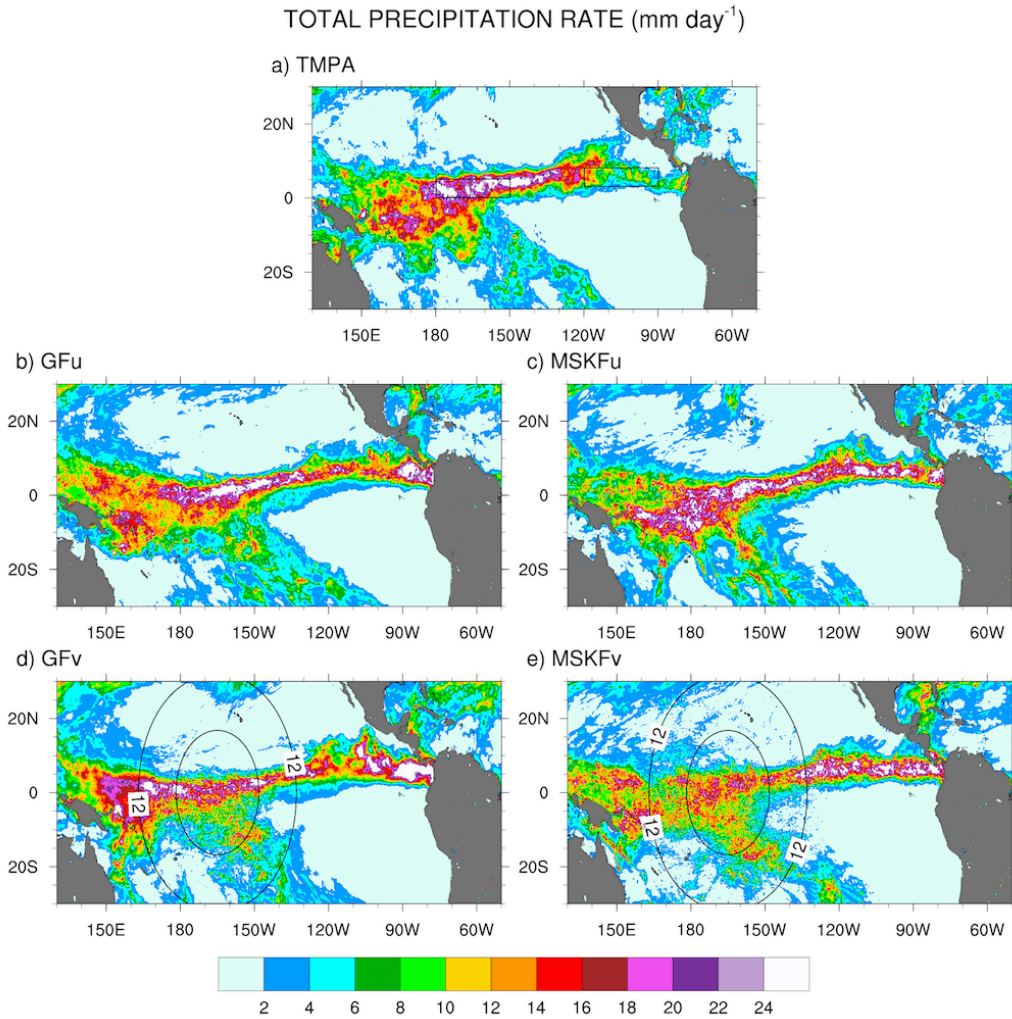


543

544 **Figure 8:** Monthly-mean convective (DEEPC) precipitation rate over the Tropical Pacific Ocean simulated in GFu and MSKFu  
 545 (top panels), GFv and MSKFv (middle panels), and ratio between the monthly-mean convective precipitation rate in GFv (MSKFv)  
 546 and GFu (MSKFu) for December 2015.

547 The simulated total precipitation rate can be compared to observed TMPA precipitation using Figs. 9 and 10  
 548 which show the precipitation rates and differences between simulated and observed precipitation rates, respectively.  
 549 Areas of maximum satellite-retrieved precipitation are found over the ITCZ between 130°W and the dateline (Fig.  
 550 9.a). Observed precipitation decreases over the warm pool west of the dateline and decreases strongly over the Tropical  
 551 Eastern Pacific (between 80°W and 120°W) and the SPCZ. The four simulations overestimate precipitation in the  
 552 Tropical Eastern Pacific between 80°W and 120°W (Figs. 9.b-e) with biases in excess of 11  $\text{mm day}^{-1}$  (Figs. 10.a-d).  
 553 The four simulations also overestimate precipitation between 130°E and 160°E, or west of the refined area, with biases  
 554 about as large as those seen east of the refined area, except for MSKFu. The uniform-grid results (Figs. 9.b-c) display  
 555 the highest precipitation rates over the area of warmest SSTs where we expect deepest convection to occur and are in

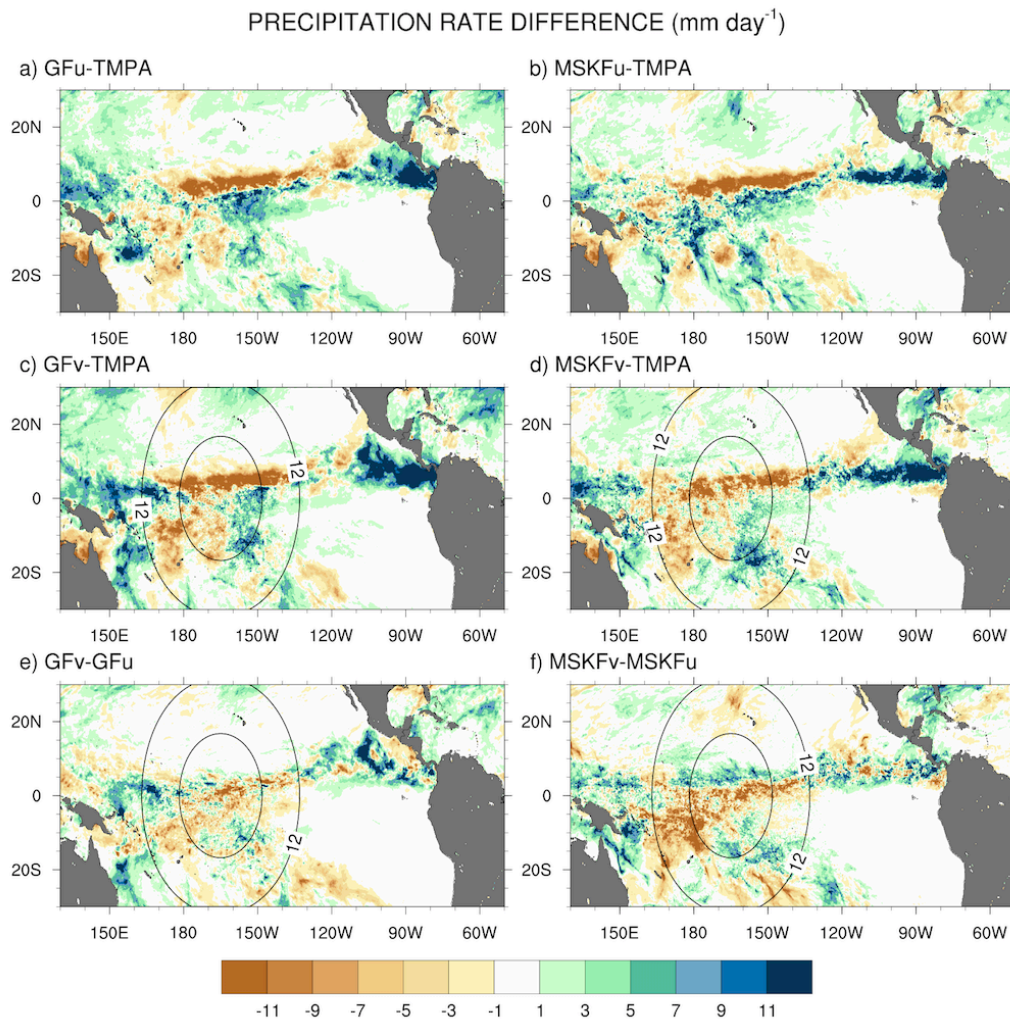
556 reasonable agreement with TMPA data. However, GFu and MSKFu locate the ITCZ south of its observed location  
 557 (Figs. 10.a-b), producing a positive bias straddling the Equator and a negative bias north of the Equator. The scale-  
 558 aware dependence of deep convection in GF leads to decreased total precipitation in GFv compared to GFu over the  
 559 entire refined area (Fig. 10.e). In contrast, Fig. 10.f shows that while the scale-aware dependence in MSKF leads to  
 560 decreased precipitation in MSKFv over a major fraction of the refined area, it also leads to an improved location of  
 561 the simulated ITCZ, as evidenced by increased precipitation north of the Equator.



562  
 563 **Figure 9:** Monthly-mean total precipitation rate over the Tropical Pacific Ocean from TMPA data (top panel) and simulated with  
 564 GFu and MSKFu (middle panels) and GFv and MSKFv (bottom panels) for December 2015.

565 Table 3 summarizes the area-mean monthly-mean convective, grid-scale, and total simulated and observed TMPA  
 566 precipitation rates over the REFINED and EAST areas. Over the two areas, the simulated total precipitation is about  
 567 the same for all four experiments but is underestimated (overestimated) relative to TMPA data over the REFINED  
 568 (EAST) areas, respectively. Over the REFINED area, total precipitation decreases by  $2.1 \text{ mm day}^{-1}$  between GFu and  
 569 GFv and  $2.3 \text{ mm day}^{-1}$  between MSKFu and MSKFv, highlighting a near-equal compensation between decreased deep  
 570 convective and increased grid-scale precipitation over the most refined area of the mesh. Over the EAST area, total  
 571 precipitation increases by  $2.7 \text{ mm day}^{-1}$  between GFu and GFv resulting from a  $5.3 (2.6) \text{ mm day}^{-1}$  increase (decrease)

572 in convective (grid-scale) precipitation. In contrast, total precipitation increases by 1.2 mm day<sup>-1</sup> between  
 573 MSKFv resulting from a 0.5 (0.6) mm day<sup>-1</sup> increase in convective (grid-scale) precipitation. The large (small) increase  
 574 in convective precipitation in GFv (MSKFv) over the coarse areas east (and west) of the refined area highlights distinct  
 575 upscaling effect of the refined area on the coarse area of the mesh between GFv and MSKFv.



576  
 577 **Figure 10:** Monthly-mean precipitation rate difference over the Tropical Pacific Ocean between GFu (MSKFu) and TMPA data  
 578 (top panels), GFv (MSKFv) and TMPA data (middle panels), and between GFv (MSKFv) and GFu (MSKFu) (bottom panels) for  
 579 December 2015.

580 In summary, the scale dependence of convection in GF and MSKF produces the same partitioning between  
 581 convective and grid-scale precipitation inside the refined area or decreased convective and compensating increased  
 582 grid-scale precipitation as horizontal resolution increases. The upscaling impact on convective and grid-scale  
 583 precipitation varies between GF and MSKF. As seen in Fig. 8 and Table 3, convective precipitation increases strongly  
 584 over the warm pool and Eastern Pacific starting across the transition zones east and west of the refined area in GFv.  
 585 In contrast, while the parameterization of the scale dependence of deep convection in MSKF produces a stronger  
 586 decrease in convective precipitation in MSKFv than GFv, it produces a smoother transition in convective precipitation  
 587 and decreased upscaling effect as spatial resolution reaches 30 km.

	CONVECTIVE (mm day <sup>-1</sup> )		GRID-SCALE (mm day <sup>-1</sup> )		TOTAL (mm day <sup>-1</sup> )	
	REFINED	EAST	REFINED	EAST	REFINED	EAST
GFu	10.0	8.7	6.1	3.7	16.1	12.4
GFv	1.9	14.0	12.1	1.1	14.0	15.1
MSKFu	10.9	10.6	4.9	4.8	15.8	15.5
MSKFv	1.7	11.1	11.8	5.4	13.5	16.5
TMPA					20.7	7.3

589 **Table 3:** Area-averaged convective, grid-scale, and total precipitation rates over the same areas as those described for Table 2. The  
590 REFINED and EAST areas are shown in Figure 9.a.

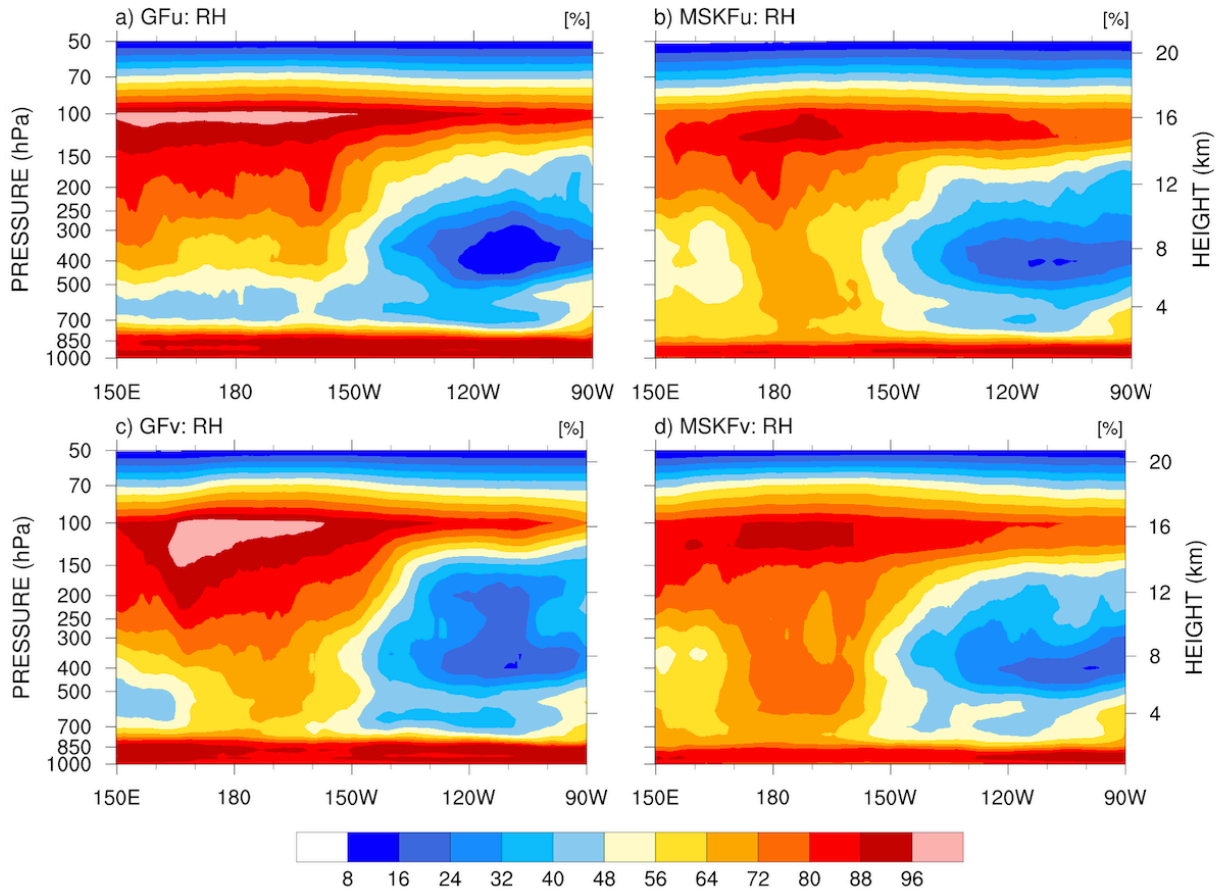
## 591 **5 Simulated relative humidity and simulated versus satellite-retrieved LWP and IWP**

### 592 **5.1 Relative humidity**

593 One effect of local mesh refinement is the decreased contribution of parameterized convection compensated by  
594 increased contribution of grid-scale cloud microphysics to condensation processes and cloud formation with  
595 increasing spatial resolution. Therefore, prior to comparing the simulated LWP and IWP against SSF data, we first  
596 investigate differences in relative humidity (RH) between our uniform- and variable-resolution experiments. Figure  
597 11 displays the monthly-mean longitude-pressure cross sections of RH latitudinally-averaged between 5°S and 5°N.  
598 East of 150°W over the Tropical Eastern Pacific, the four experiments display similar vertical distributions of RH,  
599 with relatively lower RH between 700 hPa and 150 hPa and higher RH in the PBL below 700 hPa and in the upper-  
600 troposphere above 150 hPa. All four experiments show significant increase in RH west of 150°W across the entire  
601 troposphere, over the warm pool where the warmest SSTs are seen (Fig. 2.a) and deepest convective updrafts are  
602 formed. Comparing GFu against MSKFu over the warm pool shows that GF has stronger drying than MSKF in the  
603 lower troposphere, leading to a lower RH between 850 hPa and 300 hPa in GFu than MSKFu. In addition, GF produces  
604 stronger moistening than MSKF in the upper troposphere leading to a higher RH between 300 hPa and 100 hPa in  
605 GFu than MSKFu. As seen in the bottom panels of Fig. 11, reducing parameterized deep convection while enhancing  
606 grid-scale cloud microphysics produces a higher RH over the refined area in GFv and MSKFv, but without  
607 significantly modifying RH over the coarse area of the mesh. Variations in the vertical distribution of RH at pressures  
608 less than 400 hPa are more pronounced between GFu and GFv than between MSKFv and MSKFu. Because the cloud  
609 fraction (CF) is a function of RH, as described in Xu and Randall (1996; Eq. 1), there is a strong relationship between  
610 the longitude-pressure cross sections of RH and CF, as seen in Fig. S3 (see supplemental figures). The highest CF  
611 coincide with the highest RH at about 100 hPa over the warm pool in all four experiments. As for RH, GFu and GFv  
612 display higher and lower values of CF than MSKFu and MSKFv in the upper and lower troposphere. The top and  
613 bottom panels of Fig. S4 show differences in RH and CF between GFv and GFu, and between MSKFv and MSKFu.  
614 One notable difference is a stronger increase in upper-tropospheric clouds between MSKFu and MSKFv than between

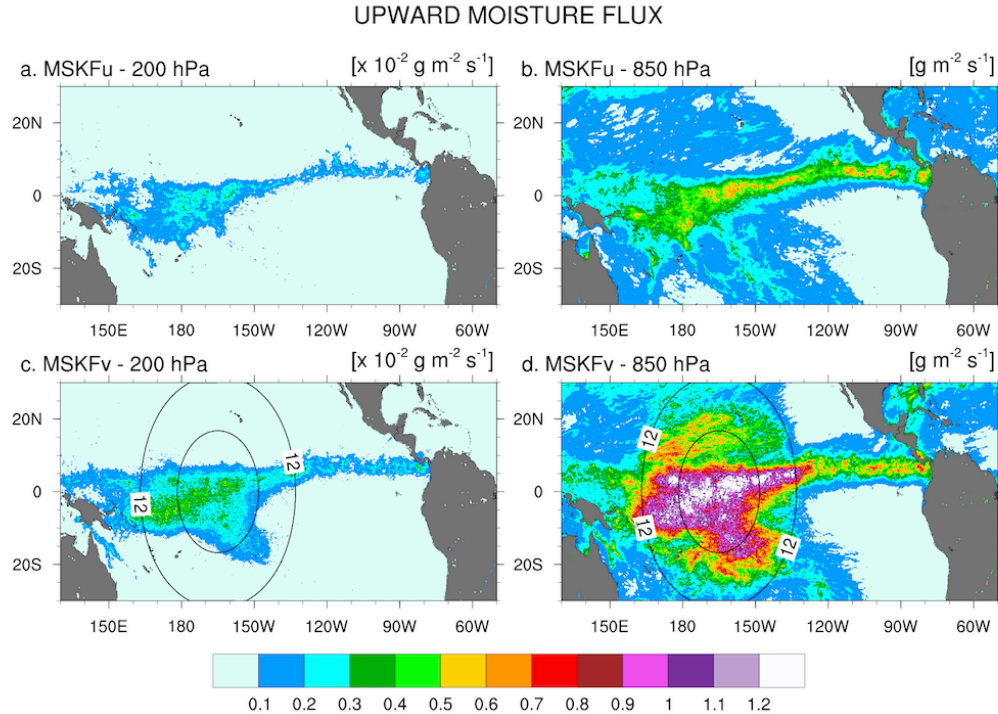


615 GFv and GFu, particularly over the refined area of the mesh. While increased grid-scale condensation over the refined  
 616 area impacts the entire troposphere in GFv, it more strongly affects the upper-troposphere in MSKFv.



617  
 618 **Figure 11:** Longitude versus pressure cross-section of latitudinally-averaged (between 5°S and 5°N) relative humidity (RH) across  
 619 the Tropical Pacific Ocean simulated in GFu and MSKFu (top panels) and GFu and GFv (bottom panels) for December 2015.

620 To explain the change in RH over the refined area between the uniform- and variable-resolution experiments, we  
 621 compare the monthly-mean upward moisture flux at 850 hPa and 200 hPa between MSKFu and MSKFv over the  
 622 Tropical Eastern Pacific (Fig. 12). There is a significant decrease in the upward moisture flux between 850 hPa and  
 623 200 hPa in conjunction with decreased specific humidity with height in MSKFu and MSKFv (Fig. 11). As seen in the  
 624 top panels of Fig. 12, MSKFu yields highest values of the upward moisture flux along the ITCZ and over the warm  
 625 pool in association with parameterized deep convection. Outside the ITCZ and warm pool, lower values of the upward  
 626 moisture flux at 850 hPa result because of reduced deep convection in conjunction with shallow convection, as seen  
 627 over the SPCZ. At increased spatial resolution, convective processes transition from being parameterized to resolved,  
 628 producing larger grid-scale vertical velocities, stronger upward moisture flux, and increased grid-scale condensation  
 629 through the entire troposphere over the refined area of the mesh. Comparing the bottom versus top panels of Fig. 12  
 630 outlines the intensification of vertical moisture transport at both pressure levels over the refined area, leading to the  
 631 increased relative humidity with increased spatial resolutions shown in Fig. 11.



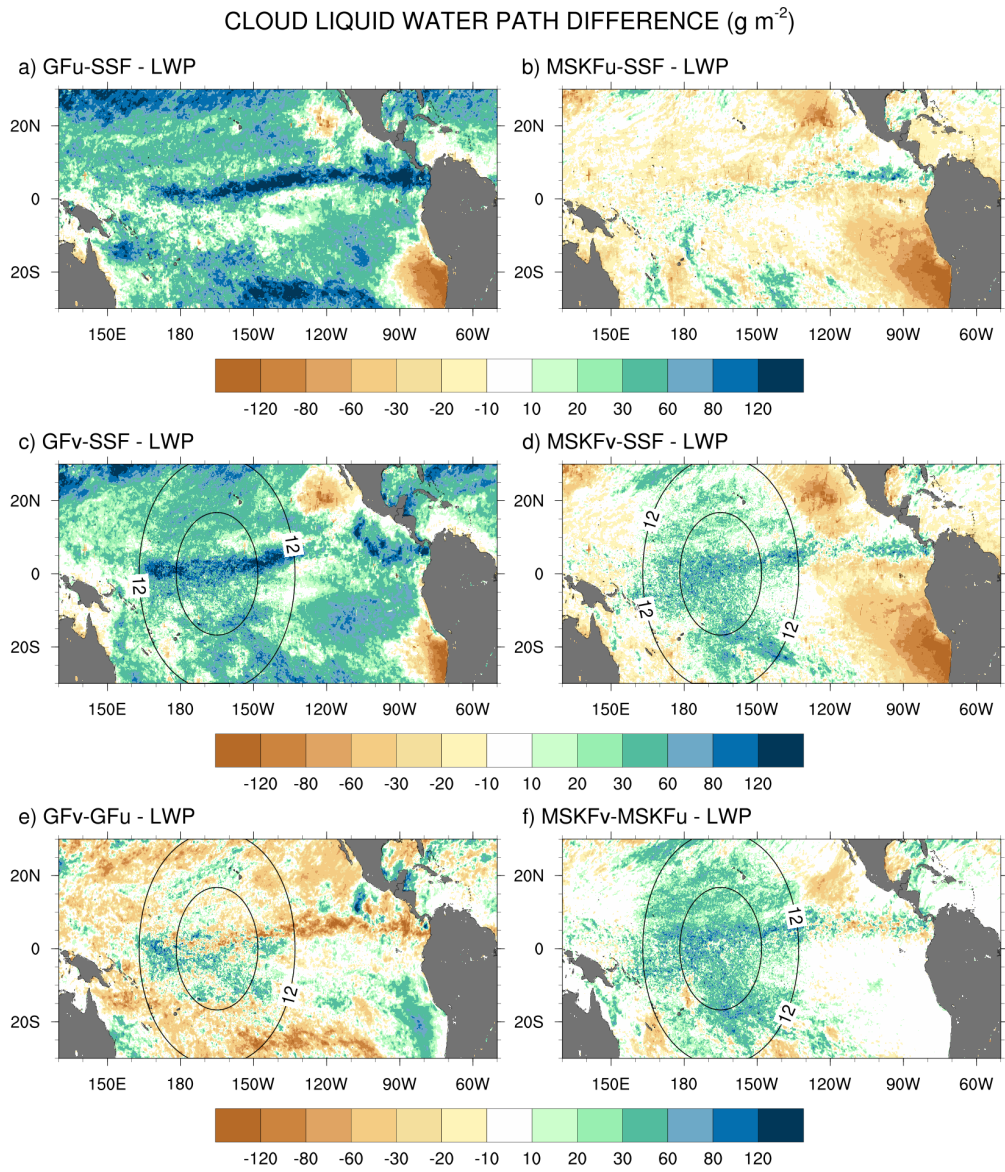
632

633 **Figure 12:** 200 hPa (left panels) and 850 hPa (right panels) monthly-mean upward moisture flux simulated with MSKF over the  
 634 Tropical Pacific Ocean for December 2015. Top panels are for MSKFu and bottom panels are for MSKFv. Note the  $1 \times 10^{-2}$  scaling  
 635 between 200 hPa and 850 hPa.

## 636 5.2 Liquid Water Path (LWP)

637 Figure 13 displays difference maps between the simulated and satellite-derived LWP, and between GFv (MSKFv)  
 638 and GFu (MSKFu). In Fig. 13, the simulated LWP is calculated using only the grid-scale cloud liquid water mixing  
 639 ratio from THOM. Separate analyses would show that adding the prognostic grid-scale rain mixing ratio to the  
 640 simulated LWP further increases biases when compared against the SSF LWP (not shown for brevity). We also did  
 641 not include the contribution of the convective cloud liquid water mixing ratio to the LWP which is small compared to  
 642 that from the grid-scale cloud microphysics. Fig. 13 highlights that GFu strongly overestimates the LWP over the  
 643 ITCZ, and between  $20^\circ\text{N}$  ( $20^\circ\text{S}$ ) and the northern (southern) limits of our analysis. As seen in Fig. 6, GFu attempts to  
 644 form low-level boundary layer clouds off the coast of Peru but these clouds form too far west from the coast when  
 645 compared against observations. This same bias is depicted in Fig 13.a since these low-level boundary layer clouds are  
 646 characterized by high LWP. In Fig. 13.b, decreased bias between the MSKFu and SSF LWP reflects that the LWP is  
 647 strongly decreased in MSKFu compared to GFu, outside of areas of low-level boundary layer clouds. If we set aside  
 648 that MSKFu is unable to simulate low-level clouds off the Baja Peninsula and coast of Peru, the magnitude and  
 649 regional patterns of the LWP simulated in MSKFu is in fairly good agreement with the SSF LWP. Because MSKF  
 650 does not allow deep and shallow convection to coexist within the same grid-cell and deep convection dominates  
 651 shallow convection over the ITCZ and warm pool, we suggest that detrained cloud water from deep convection as a  
 652 source to grid-scale microphysics contributes a major part to the LWP produced by MSKFu. The bottom panels of  
 653 Fig. 13 reveal that the mesh refinement impacts the LWP simulated with MSKF more effectively than that simulated

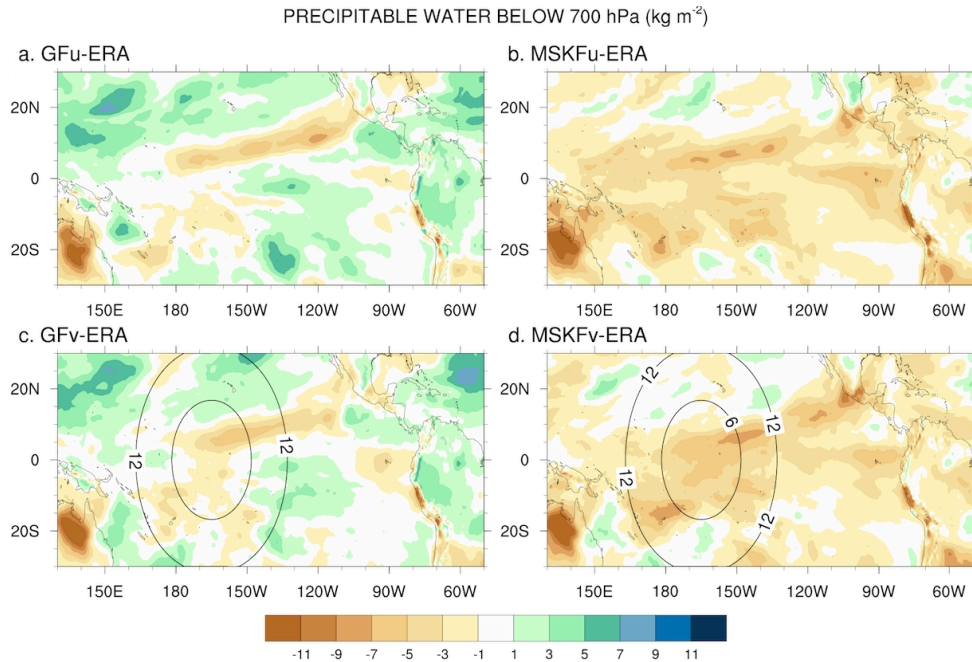
654 with GF inside the refined area. This result is in agreement with the stronger increase in RH between MSKFu and  
 655 MSKFv than between GFu and GFv at lower levels. MSKFv yields an increased LWP relative to MSKFu over the  
 656 entire refined area (Fig. 13.f). MSKFv also has increased LWP compared to MSKFu over the coarse area, but not as  
 657 large as that seen over the refined area. Fig. 13.e shows that LWP differences do not have a strong positive or negative  
 658 trend inside the refined area, due to the fact that GF allows deep and shallow convection to coexist within the same  
 659 grid-cell of deepest convective activity, mainly over the ITCZ and warm pool, and shallow convection does not  
 660 account for variations in horizontal grid-spacing. Over the coarse area, an obvious decrease in the LWP between GFv  
 661 and GFu is seen over the ITCZ in the Tropical Eastern Pacific as well as along the southern boundary of our analysis.



662  
 663 **Figure 13:** Monthly-mean cloud liquid water path (LWP) difference over the Tropical Pacific Ocean between GFu (MSKFu) and  
 664 SSF data (top panels), GFv (MSKFv) and SSF data (middle panels), and monthly-mean LWP difference between GFv (MSKFv)  
 665 and GFu (MSKFu) (bottom panels) for December 2015.

666 In order to investigate the reasons why the LWP simulated in GFu strongly exceeds that from the SSF products  
667 and MSKFu, we calculated the monthly-mean LWP produced in grid-cells with incidence of deep convection, shallow  
668 convection, and no convection, using LWP hourly outputs from GFu. Separate maps would show that a major fraction  
669 of the LWP over convectively active regions such as the ITCZ is actually produced at times when no convection is  
670 active or when only shallow convection is triggered. In GF, and in contrast to deep convection, shallow convection  
671 detrains total water as a source of grid-scale water vapor instead of detraining water vapor, cloud liquid and ice water,  
672 separately. Because the detrained total water is treated as a source of water vapor, supersaturation conditions are more  
673 likely to persist and later removed by grid-scale condensation. In contrast, detrainment from deep convective updrafts  
674 acts as a source of liquid water if temperatures are warmer than 258 K. Deep convection in conjunction with grid-  
675 scale condensation contributes the least to the LWP because updrafts are taller and their cloud-top temperatures colder  
676 than those from shallow convection, leading to condensation and deposition to occur at levels where temperatures are  
677 colder than 258 K, and where ice phase processes dominate.

678 The impact of more active shallow convection in GFu (GFv) than in MSKFu (MSKFv) is analyzed using Fig. 14  
679 which shows differences in the monthly-mean precipitable water below 700 hPa between our experiments and ERA-  
680 Interim reanalyses. Because varying horizontal resolution does not affect shallow convection, GFv (MSKFv) displays  
681 similar biases as GFu (MSKFu) over the entire analysis domain, including the refined area. Comparing the left versus  
682 right panels of Figure 14 reveals that the precipitable water simulated in GFu (GFv) displays a positive bias whereas  
683 that simulated in MSKFu (MSKFv) displays a negative bias in the lower troposphere relative to ERA-Interim data,  
684 mainly over areas of shallow convection. In GF, the abundance of shallow convection (Figure 6.a, Figure 6.c)  
685 associated with detrained total water acting as a source of grid-scale water vapor promotes the lower troposphere to  
686 stay more humid and cloud liquid water to form more often than actually observed (Figure 13.a, Figure 13.c), north  
687 and south of the ITCZ and warm pool. In MSKF, while shallow convection is as widespread over the Tropical Pacific  
688 Ocean as in GF, it cannot act as a major source of detrained total water to the grid-scale microphysics because it is not  
689 triggered as often as deep convection. In addition, because MSKF partitions detrained water into water vapor, cloud  
690 water, cloud ice, rain, and snow, instead of detraining total water in the form of water vapor as in GF, the amounts of  
691 available water vapor and cloud liquid water are reduced relative to GF.



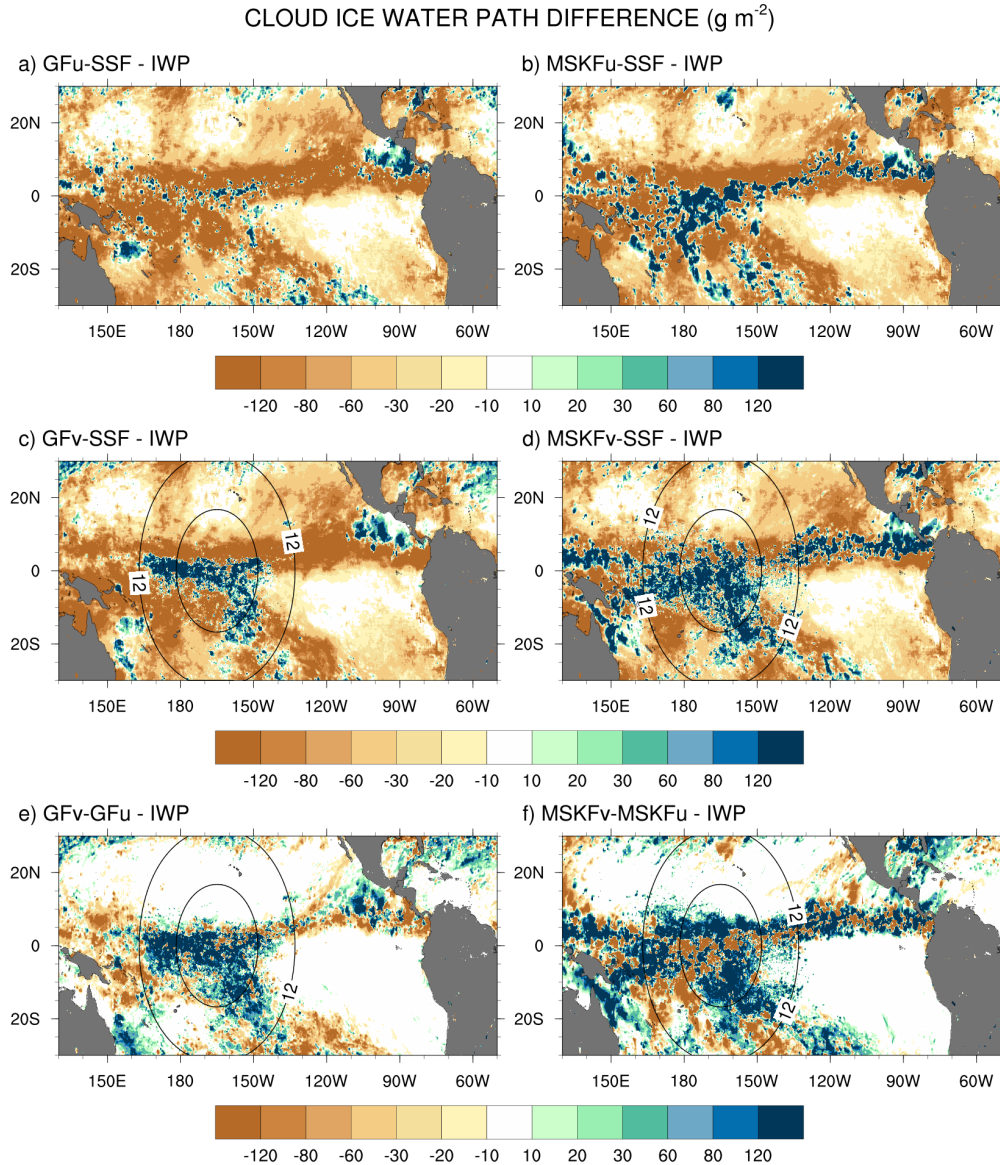
692

693 **Figure 14:** Monthly-mean difference between the simulated and ERA-Interim precipitable water below 700 hPa over the Tropical  
 694 Pacific Ocean for December 2015.

695 **5.3 Ice Water Path (IWP)**

696 Because MODIS is relatively insensitive to precipitation, the simulated IWP should comprise cloud ice, snow,  
 697 and graupel. Because graupel contributes a minor part to the IWP relative to cloud ice and snow and our results  
 698 highlight strong biases against SSF data, we do not include graupel in our computation of the simulated IWP. It is also  
 699 important to note that because THOM has the propensity to rapidly convert cloud ice to snow (Thompson et al. 2016),  
 700 most of the IWP is in the form of snow which falls at higher speeds than cloud ice, enhancing the depth of ice clouds.  
 701 Lastly, the middle panels of Fig. 5 show that our gridding of the IWP orbital data produce increased monthly mean  
 702 IWP than the official SSF1deg product. This result implies that biases between the simulated and satellite-derived  
 703 IWP will be underestimated when using our SSF  $0.2^\circ \times 0.2^\circ$  IWP data. Figure 15 shows difference maps between the  
 704 simulated and satellite-derived IWP, and between GFv (MSKFv) and GFu (MSKFu). When compared against the SSF  
 705 IWP, GFu is the only experiment that mostly underestimates the IWP along the ITCZ and warm pool whereas GFv  
 706 yields a strong increase in the IWP over the refined area of the mesh relative to GFu. Both GFu and GFv overestimate  
 707 the IWP along the west coast of Central America, as they did for the LWP and precipitation. Comparing MSKFu  
 708 (MSKFv) against GFu (GFv) shows that MSKF leads to increased positive biases in the IWP compared to GF over  
 709 the entire ITCZ and warm pool. Increased convective detrainment of cloud ice as a source of grid-scale cloud ice to  
 710 THOM in MSKF than in GFv, because partitioning between cloud liquid and ice water starts at warmer temperatures,  
 711 may be responsible to the increased IWP. The bottom panels of Figure 15 reveal that increasing spatial resolution  
 712 worsens the simulated IWP compared to the SSF IWP over the refined area in GFv and MSKFv. As shown in Fig. 11,  
 713 mesh refinement over the warm pool yields higher upper-tropospheric relative humidity leading to increased ice cloud

714 microphysics. In contrast to GFv, MSKFv displays an increase in the IWP over the coarse area of the mesh, showing  
 715 a stronger impact of the refined area on the coarse area of the mesh in MSKFv than GFv in the upper-troposphere.



716  
 717 **Figure 15:** As Fig. 13, but for the cloud ice water path (IWP).

718 **5.4 TOA radiation budget**

719 Biases in the LWP and IWP introduce biases in the cloud fraction and cloud optical properties which in turn lead  
 720 to biases in the simulated TOALW and TOASW compared to CERES-SSF data. Figures S5, S6, and S7 display the  
 721 monthly-mean CF, TOALW, and TOASW from SSF data for December 2015 and the differences between the model  
 722 results and observations. Focusing on areas of deep convection over the ITCZ and warm pool, all four simulations  
 723 overestimate CF with larger biases seen in the GF than the MSKF experiments, and larger biases seen in the variable-  
 724 resolution than the uniform-resolution experiments. All four simulations also overpredict CF along the west coast of  
 725 Central America while underpredicting CF over areas of stratiform clouds along the west coast of South America and

726 Baja Peninsula. The impact of CF biases is that all four experiments underestimate the size of the warm pool and  
727 width of the ITCZ, leading the TOALW (TOASW) to be too high (low) over areas of deep convection. These  
728 differences are clearly linked to the differences noted in the LWP and IWP between MPAS and SSF data.

## 729 **6 Discussion and future research**

730 Uniform- and variable-resolution experiments with two scale-aware parameterizations of deep convection (GF  
731 and MSKF) in MPAS yield significant biases between the simulated and satellite-derived monthly-mean precipitation  
732 rates, LWP, IWP, and CF over the Tropical Pacific Ocean for December 2015. In turn, biases affect the cloud fraction  
733 and optical properties producing significant differences in the TOALW and TOASW compared to CERES-SSF data.

734 Tropical precipitation simulated with uniform-resolution experiments is overestimated compared to TMPA, due  
735 to subgrid-scale deep convection. Biases using GF are as large as those using MSKF, and result in part because the  
736 simulated ITCZ is located south of its observed location. Variable-resolution experiments do not produce significant  
737 improvement in simulating precipitation against TMPA. Inside the refined area, decreased convective precipitation  
738 plus compensating increased grid-scale precipitation have the simulated total precipitation to exhibit similar biases  
739 between the uniform- and variable-resolution experiments with GF and MSKF. One major difference in using GF  
740 instead of MSKF is the strong upscaling effect of the refined mesh on the coarse mesh, producing a strong increase in  
741 convective precipitation east and west of the refined mesh. Because deep convection does not exhibit similar behaviour  
742 over the transition zone between the coarse and refined areas of the mesh in MSKF, we plan further to investigate this  
743 difference in convective precipitation in terms of the size of convective updrafts as a function of horizontal resolution  
744 and increased moistening of the lower troposphere from shallow convection.

745 Differences in the simulated LWP between the uniform- and variable-resolution experiments using GF and MSKF  
746 and against the CERES-SSF LWP highlight the need to revise the treatment of shallow convection to improve warm-  
747 phase clouds in both schemes. While experiments using MSKF yield the simulated LWP to be in reasonable agreement  
748 against that from the CERES-SSF product, those using GF yield the simulated LWP to be strongly overestimated.  
749 Analyses show that shallow convection and cloud microphysics processes explain most of the increased LWP in GFu  
750 and GFv compared to MSKFu and MSKFv, and satellite-derived data. We plan to update the GF shallow convection  
751 scheme with that implemented in version 4.1 of the Advanced Research Weather Forecast (WRF) model. Because the  
752 updated scheme includes an improved cloud model that allows water vapor and cloud liquid water to detrain separately  
753 and a fraction of condensed water to precipitate, we will focus on the impact of explicit detrainment of cloud liquid  
754 water and precipitation from shallow convective updrafts on the simulated LWP in GF. Results show that MSKF  
755 underestimates shallow convection, leading the troposphere below 700 hPa to be drier than actually observed. These  
756 results imply that the shallow convection in MSKF needs to be updated or that a separate parameterization of shallow  
757 convection needs to be used in addition to that in MSKF. Using the same parameterization of shallow convection, and  
758 partitioning of the detrained condensed water between cloud liquid water and ice in GF and MSKF, will further provide  
759 understanding in the partitioning of the LWP between subgrid-scale deep and shallow convection. Variable-resolution  
760 experiments strongly overestimate the IWP compared to CERES-SSF data over the refined area of the mesh, leading  
761 to strong biases in the cloud fraction, and TOA long- and short-wave radiation. Because subgrid-scale deep convection

762 is reduced at increased horizontal resolutions, grid-scale cloud microphysics contributes a major part to biases in the  
763 simulated IWP.

764       Parameterizing the dependence of subgrid-scale deep convection as a function of horizontal resolution allows the  
765 use of variable-resolution meshes spanning between hydrostatic and nonhydrostatic scales within a global framework  
766 for regional NWP and climate experiments. Although deep convection is not fully explicitly resolved over the refined  
767 area of the mesh in our variables-resolution experiments, it is substantially reduced relative to that over the coarse area  
768 of the mesh, allowing to contrast the contribution of subgrid-scale convection and cloud microphysics processes. As  
769 horizontal resolution increases from the coarse to refined area of the mesh, deep convection gradually transitions from  
770 parameterized to resolved and cloud microphysics contribute a major part to moist processes over the refined mesh.  
771 Shallow convection coupled with grid-scale microphysics contributes a major part to the low-level cloud liquid water  
772 and mixed-phase clouds whereas grid-scale cloud microphysics contribute a major part to the formation of upper-  
773 tropospheric ice clouds over the refined area. Our results show that mesh refinement does not systematically improve  
774 precipitation and clouds over the Tropical Pacific Ocean as grid-scale condensation increases at increased resolutions.  
775 As cloud microphysics processes drive the moisture budget over the refined area of the mesh, we propose to expand  
776 this diagnostic study to a process study by further understanding the cloud microphysics processes that need to be  
777 improved in order to reduce discrepancies between model and observations. In that vein, the recently developed MSKF  
778 that includes a double moment microphysics (Glotfelty et al., 2019) would be useful in a future process study.

779  
780

781 *Code and data availability:* The source code used to initialize and run our experiments is based on MPAS-v5.2 which  
782 is freely available from <https://github.com/MPAS-Dev/MPAS-Model/releases/tag/v5.2>. Modifications to the original  
783 source code and scripts to run the experiments are available from <https://doi.org/10.5281/zenodo.3515440> (Fowler,  
784 2019) while initialization files, and outputs from the experiments are located on the NCAR Campaign Storage System.  
785 These files can be made available by contacting the corresponding author. Examples of CERES SSF Aqua and Terra  
786 orbital and gridded data, daily-mean and monthly-mean simulated diagnostics, and post-processing scripts are also  
787 available from <https://doi.org/10.5281/zenodo.3515440> (Fowler, 2019).

788  
789

790 *Author contributions:* LF developed all the modifications that were made to the MPAS-v5.2 released version and were  
791 necessary to run the different experiments. KA made all the updates to the MultiScale Kain-Fritsch parameterization  
792 of convection. LF and MB designed the experiments, and LF conducted and analyzed the simulations. LF prepared  
793 the manuscript with contributions from all co-authors.

794  
795

796 *Competing interests:* The authors declare that they have no conflict of interest.

797  
798



799 *Acknowledgments:* This research is based upon work supported by the National Center for Atmospheric Research  
800 which is a major facility sponsored by the National Science Foundation under Cooperative Agreement No. 1852977.  
801 The authors thank Dr. Hugh Morrison for his careful review and constructive suggestions of the manuscript prior to  
802 its submission. The CERES-SSF data were obtained from the NASA Langley Research Center Atmospheric Science  
803 Data Center. The TMPA data were acquired as part of the activities of NASA's Science Mission Directorate and are  
804 archived and distributed by the Goddard Earth Sciences (GES) Data and Information Services Center (DISC). We  
805 would like to acknowledge high-performance computing support from Cheyenne (doi:10.5065/D6RX99hX) provided  
806 by NCAR's Computational and Information Systems Laboratory, sponsored by the National Science Foundation. We  
807 acknowledge the use of the NCAR Command Language (Version 6.3.2) [Software]. (2019). Boulder, Colorado:  
808 UCAR/NCAR/CISL/TDD. <http://dx.doi.org/10.5065/D6WD3XH5> for all figures.

809

## References

- 810 Alapaty, K., Herwehe, J.A., Otte, T.L., Nolte, C.G., Bullock, O.R., Ballard, M.S., Kain, J.S., and Dudhia, J.:  
811 Introducing subgrid-scale cloud feedbacks to radiation for regional meteorological and climate modeling,  
812 *Geophys. Res. Lett.*, 39, L24809, <https://doi.org/10.1029/2012GL054031>, 2012.
- 813 Alishouse, J.C., Snider, J.B., Westwater, E.R., Swift, C.T., Ruf, C.S., Vongsathron, S.A., and Ferraro, R.R.:  
814 Determination of cloud liquid water content using the SSM/I, *IEEE T. Geosci. Remote*, 28, 817-822,  
815 <https://doi.org/10.1109/36.58968>, 1990.
- 816 Arakawa, A., and Schubert, W.H.: Interaction of a cumulus cloud ensemble with the large-scale environment, Part I,  
817 *J. Atmos. Sci.*, 31, 674-701, [https://doi.org/10.1175/1520-0469\(1974\)031<0674:IOACCE>2.0.CO;2](https://doi.org/10.1175/1520-0469(1974)031<0674:IOACCE>2.0.CO;2), 1974.
- 818 Arakawa, A., and Wu, C.-M.: A unified representation of deep moist convection in numerical modeling of the  
819 atmosphere. Part I, *J. Atmos. Sci.*, 70, 1977-1992, <https://doi.org/10.1175/JAS-D-12-0330.1>, 2013.
- 820 Bechtold, P., Bazile, E., Guichard, F., Mascart, P., and Richard, E.: A mass-flux convection scheme for regional and  
821 global models, *Q. J. Roy. Meteor. Soc.*, 130, 3139-3172, <https://doi.org/10.1002/qj.49712757309>, 2001.
- 822 Bechtold, P., Köhler, M., Jung, T., Doblas-Reyes, F., Leutbecher, M., Rodwell, M. J., Vitart, F., and Balsamo, G.:  
823 Advances in simulating atmospheric variability with the ECMWF model: From synoptic to decadal time-scales,  
824 *Q. J. Roy. Meteor. Soc.*, 134, 1337–1351, <https://doi.org/10.1002/qj.289>, 2008.
- 825 Brown, J.M.: Mesoscale unsaturated downdrafts driven by rainfall evaporation: A numerical study, *J. Atmos. Sci.*, 36,  
826 313-338, [https://doi.org/10.1175/1520-0469\(1979\)036<0313:MUDDBR>2.0.CO;2](https://doi.org/10.1175/1520-0469(1979)036<0313:MUDDBR>2.0.CO;2), 1979.
- 827 Chen, F., and Dudhia, J.: Coupling an advanced land surface-hydrology model with the Penn State-NCAR MM5  
828 modeling system. Part I: Model implementation and sensitivity, *Mon. Weather Rev.*, 129, 569-585,  
829 [https://doi.org/10.1175/1520-0493\(2001\)129<0569:CAALSH>2.0.CO;2](https://doi.org/10.1175/1520-0493(2001)129<0569:CAALSH>2.0.CO;2), 2001.
- 830 Dee, D.P., and 35 co-authors: The ERA-Interim reanalysis: configuration and performance of the data assimilation  
831 system, *Q. J. Roy. Meteor. Soc.*, 137, 553-597, <https://doi.org/10.1002/qj.828>, 2011.
- 832 Dolinar, E.K., Dong, X., Xi, B., Jiang, J.H., and Su, H.: Evaluation of CMIP5 simulated clouds and TOA radiation  
833 budgets using NASA satellite observations, *Clim. Dynam.*, 44, 2229-2247, [https://doi.org/10.1007/s00382-014-](https://doi.org/10.1007/s00382-014-2158-9)  
834 [2158-9](https://doi.org/10.1007/s00382-014-2158-9), 2015.
- 835 Fowler, L.D., Skamarock, W.C., Grell, G.A., Freitas, S.R., and Duda, M.G.: Analyzing the Grell-Freitas convection  
836 scheme from hydrostatic to nonhydrostatic scales within a global model, *Mon. Weather Rev.*, 144, 2285-2306,  
837 <https://doi.org/10.1175/MWR-D-15-0311.1>, 2016.
- 838 Frank, W.M., and Cohen, C.: Simulation of tropical convective systems. Part I: A cumulus parameterization, *J. Atmos.*  
839 *Sci.*, 44, 3787-3799, [https://doi.org/10.1175/1520-0469\(1987\)044<3787:SOTCSP>2.0.CO;2](https://doi.org/10.1175/1520-0469(1987)044<3787:SOTCSP>2.0.CO;2), 1987.

840 Fritsch, J.M., and Chappell, C.F.: Numerical prediction of convectively driven mesoscale pressure systems. Part I:  
841 Convective parameterization, *J. Atmos. Sci.*, 37, 1722–1733, [https://doi.org/10.1175/1520-0469\(1980\)037<1722:NPOCDM>2.0.CO;2](https://doi.org/10.1175/1520-0469(1980)037<1722:NPOCDM>2.0.CO;2), 1980.

843 Fowler, L.D.: experimentsMPAS-v5.2, Zenodo, <https://doi.org/10.5281/zenodo.3515440>, 2019.

844 Geier, E.B., Green, R.N., Kratz, D.P., Minnis, P., Miller, W.F., Nolan, S.K., and Franklin, C.B.: Clouds and the Earth’s  
845 Radiant Energy System (CERES) data management system. Single Satellite Footprint TOA/Surface Fluxes and  
846 Clouds (SSF) collection document. Release 2, Version 1, 243 pp, 2003.

847 Giorgetta, M.A., Brokopf, R., Crueger, T., Esch, M., Fiedler, S., Helmert, J., Hohenegger, C., Kornblueh, L., Köhler,  
848 M., Manzini, E., Mauritsen, T., Nam, C., Raddatz, T., Rast, S., Reinert, D., Sakradzija, M., Schmidt, H., Schneck,  
849 R., Schnur, R., Silvers, L., Wan, H., Zängl, G., and Stevens, B: ICON-A, the atmosphere component of the ICON  
850 Earth System Model: I. Model description, *J. Adv. Model. Earth Sy.*10, 1613-1637,  
851 <https://doi.org/10.1029/2017MS001242>, 2018.

852 Glotfelty, T., Alapaty, K., He, J., Hawbecker, P., Song, X., and Zhang, G.: The Weather Research and Forecasting  
853 Model with aerosol cloud-interactions (WRF-ACI): Development, evaluation, and initial applications, *Mon. Wea.*  
854 *Rev.*, 147, 1491-1511, <https://doi.org/10.1175/MWR-D-18-0267.1>, 2019.

855 Greenwald, T.J., Stephens, G.L., Vonder Haar, T.H., and Jackson, D.L.: A physical retrieval of cloud liquid water  
856 over global oceans using special sensor microwave/imager (SSM/I) observations, *J. Geophys. Res.*, 98, 18471-  
857 18488, <https://doi.org/10.1029/93JD00339>, 1993.

858 Grell, G.A: Prognostic evaluation of assumptions uses by cumulus parameterizations, *Mon. Weather Rev.*, 121, 764-  
859 787, [https://doi.org/10.1175/1520-0493\(1993\)121<0764:PEOAUB>2.0.CO;2](https://doi.org/10.1175/1520-0493(1993)121<0764:PEOAUB>2.0.CO;2), 1993.

860 Grell, G.A., and Dévényi, D.: A generalized approach to parameterizing convection combining ensemble and data  
861 assimilation techniques, *Geophys. Res. Lett.*, 29, 38-1-38-4, <https://doi.org/10.1029/2002GL015311>, 2002.

862 Grell, G.A., and Freitas, S.R.: A scale and aerosol aware stochastic parameterization for weather and air quality  
863 modeling, *Atmos. Chem. Phys.*, 14, 5233-5250, <https://doi.org/10.5194/acp-14-5233-2014>, 2014.

864 Guo, H., Golaz, J.-C., Donner, L., Wyman, B., Zhao, M., and Ginoux, P.: CLUBB as a unified cloud parameterization:  
865 opportunities and challenges, *Geophys. Res. Lett.*, 42, 4540-4547, <https://doi.org/10.1002/2015GL063672>, 2015.

866 He, J., and Alapaty, K.: Precipitation partitioning in multiscale atmospheric simulations: Impacts of stability  
867 restoration methods, *J. Geophys. Res.*, 123, 10185-10201, <https://doi.org/10.1029/2018JD028710>, 2018.

868 Herwehe, J.A., Alapaty, K., and Bullock Jr., O.R: Evaluation of developments toward a multi-scale Kain-Fritsch  
869 parameterization in WRF. 2014 Community Modeling and Analysis System Conference, Chapel Hill, NC, EPA,  
870 2014.

871 Hong, S.-Y., and Lim, J.-O: The WRF single moment 6-class microphysics scheme (WSM6), *J. Korean Meteor. Soc.*,  
872 42, 129-151, 2006.

873 Hong, S.-Y., Choi, J., Chang, E.-C., Park, H., and Kim Y.-J.: Lower-tropospheric enhancement of gravity wave drag  
874 in a global spectral atmospheric forecast model, *Weather Forecast*, 23, 523-531,  
875 <https://doi.org/10.1175/2007WAF2007030.1>, 2008.

876 Huffman, G.J., Balvin, D.T., Nelkin, E.J., and Wolff, D.B.: The TRMM Multisatellite Precipitation Analysis (TMPA):  
877 Quasi-global, multiyear, combined-sensor precipitation at fine scales, *J. Hydrometeorol.*, 8, 38-55,  
878 <https://doi.org/10.1175/JHM560.1>, 2007.

879 Iacono, M. J., Mlawer, E. J., Clough, S. A., and Morcrette, J.-J.: Impact of an improved longwave radiation model,  
880 RRTM, on the energy budget and thermodynamic properties of the NCAR Community Climate Model, CCM3,  
881 *J. Geophys. Res.*, 105, 14 873–14 890, <https://doi.org/10.1029/2000JD900091>, 2000.

882 Jiang, J.H., Su, H., Zhai, C., Perun, V.S, Del Genio, A., Nazarenko, L.S., Donner, L.J., Horowitz, L., Seman, C., Cole,  
883 J., Gettelman, A., Ringer, M.A., Rotstayn, L., Jeffrey, S., Wu, T., Brient, F., Dufresne, J.-L., Kawai, H., Koshiro,  
884 T., Watanabe, M., L’Ecuyer, T.S., Volodin, E.M., Iversen, T., Drange, H., Mesquita, M.D.S., Read, W.G., Waters,  
885 J.W., Tian, B., Teixeira, J., and Stephens, G.L.: Evaluation of cloud and water vapor simulations in CMIP5  
886 climate models using NASA “A-Train” satellite observations, *J. Geophys. Res.*, 117, D14105,  
887 <https://doi.org/10.1029/2011JD017237>, 2012.

888 Ju, L., Ringler, T., and Gunzburger, M.: Voronoi tessellations and their applications to climate and global modeling,  
889 *Numerical Techniques for Global Atmospheric Models*, P. Lauritzen et al., Eds., Springer, 313-342, 2011.

890 Kain, J.S.: The Kain-Fritsch parameterization: An update, *J. Appl. Meteorol.*, 43, 170-181,  
891 [https://doi.org/10.1175/1520-0450\(2004\)043<0170:TKCPAU>2.0.CO;2](https://doi.org/10.1175/1520-0450(2004)043<0170:TKCPAU>2.0.CO;2), 2004.

892 Kain, J.S, and Fritsch, J.M.: A one-dimensional entraining/detraining plume model and its application in convective  
893 parameterization, *J. Atmos. Sci.*, 47, 2784-2802, [https://doi.org/10.1175/1520-0469\(1990\)047<2784:AODEPM>2.0.CO;2](https://doi.org/10.1175/1520-0469(1990)047<2784:AODEPM>2.0.CO;2), 1990.

895 Kain, J.S., and Fritsch, J.M.: The role of convective “trigger function” in numerical forecasts of mesoscale convective  
896 systems, *Meteorol. Atmos. Phys.*, 49, 93-106, <https://doi.org/10.1007/BF01025402>, 1992.

897 Kain, J.S., and Fritsch, J.M.: Convective parameterization for mesoscale models: The Kain-Fritsch scheme, *The*  
898 *Representation of Cumulus Convection in Numerical Models*, Meteor. Mon., No. 24, American Meteorological  
899 Society, Boston, MA, 165-170, [https://doi.org/10.1007/978-1-935704-13-3\\_16](https://doi.org/10.1007/978-1-935704-13-3_16), 1993.

900 Kay, J.E., Deser, C., Phillips, A., Mai, A., Hannary, C., Strand, G., Arblaster, J.M., Bates, S.C., Danabasoglu, G.,  
901 Edwards, J., Holland, M., Kushner, P., Lamarque, J.-F., Lawrence, D., Lindsay, K., Middleton, A., Munoz, E.,  
902 Neale, R., Oleson, K., Polvani, L., and Vertenstein, M.: The Community Earth System Model (CESM) large  
903 ensemble project, *B. Am. Meteorol. Soc.*, 96, 1333-1349, <https://doi.org/10.1175/BAMS-D-13-00255.1>, 2015.

904 Kessler, E.: On the distribution and continuity of water substances in atmospheric circulation, *Meteor. Mon.*, No. 10,  
905 American Meteorological Society, Boston, MA, 1-84, [https://doi.org/10.1007/978-1-935704-36-2\\_1](https://doi.org/10.1007/978-1-935704-36-2_1), 1969.

906 Klemp, J.B.: A terrain-following coordinate with smoothed coordinate surfaces, *Mon. Weather Rev.*, 139, 2163-2169,  
907 <https://doi.org/10.1175/MWR-D-10-05046.1>, 2011

908 Klemp, J.B., Skamarock, W.C., and Dudhia, J.: Conservative split-explicit time integration methods for the  
909 compressible nonhydrostatic equations, *Mon. Weather Rev.*, 135, 2897-2913,  
910 <https://doi.org/10.1175/MWR3440.1>, 2007.

911 Krishnamurti, T.N., Low-Nam, S., and Pasch, R.: Cumulus parameterization and rainfall rates II, *Mon. Weather Rev.*,  
912 111, 815-828, [https://doi.org/10.1175/1520-0493\(1983\)111<0815:CPARRI>2.0.CO;2](https://doi.org/10.1175/1520-0493(1983)111<0815:CPARRI>2.0.CO;2), 1983.

913 Li, J.-L., Waliser, D., Woods, C., Teixeira, J., Bacmeister, J., Chern, J., Shen, B.-W., Tompkins, A., Tao, W.-K., and  
914 Köhler, M.: Comparisons of satellites liquid water estimates to ECMWF and GMAO analyses, 20<sup>th</sup> century IPCC  
915 AR4 climate simulations and GCM simulations, *Geophys. Res. Lett.*, 35, L9710,  
916 <https://doi.org/10.1029/2008GL035427>, 2008.

917 Li, J.-L., Waliser, D.E., Chen, W.-T., Guan, B., Kubar, T., Stephens, G., Ma, H.-Y., Deng, M., Donner, L., Seman, C.,  
918 , and Horowitz, L.: An observational based evaluation of cloud ice water in CMIP3 and CMIP5 GCMs and  
919 contemporary reanalyses using contemporary satellite data, *J. Geophys. Res.*, 117, D16105,  
920 <https://doi.org/10.1029/2012JD017640>, 2012.

921 Li, J.-L., Lee, S., Ma, H.-Y., Stephens, G., and Guan, B.: Assessment of the cloud liquid water from climate models  
922 and reanalysis using satellite observations, *Terr. Atmos. Ocean. Sci.*, 29(6), 653-678,  
923 <https://doi.org/10.3319/TAO.2018.07.04.01>, 2018.

924 Mahoney, K.M.: The representation of cumulus convection in high-resolution simulations of the 2013 Colorado front  
925 range flood, *Mon. Weather Rev.*, 144, 4265-4278, <https://doi.org/10.1175/MWR-D-16-0211.1>, 2016.

926 Meehl, G.A., Delworth, T.L., Latiff, M., McAveney, B., Mitchell, J.F.B., Stouffer, R.J., and Taylor, K.E.: The WCRP  
927 CMIP3 multimodel dataset: A new era in climate change research, *B. Am. Meteorol. Soc.*, 88, 1383-1394,  
928 <https://doi.org/10.1175/BAMS-88-9-1383>, 2007.

929 Minnis, P., and coauthors: CERES Edition-2 cloud property retrievals using TRMM VIRS and Terra and Aqua  
930 MODIS data-Part I: Algorithms, *IEEE T. Geosci. Remote.*, Vol. 49, NO 11, 4374-4400,  
931 <https://doi.org/10.1109/TGRS.2011.2144601>, 2011.

932 Minnis, P., Kratz, D.P., Coakley, J.J.A., King, M.D., Garber, D., Heck, P., Mayor, S., Young, D.F., and Arduini, R.:  
933 Cloud optical property retrieval (Subsystem 4.3), in *Clouds and the Earth's Radiant Energy System (CERES)*  
934 *Algorithm Theoretical Basis Document*, Vol III, Clouds and Radiance Inversions (Subsystem 4), NASA RP  
935 1376, edited by Science Team CERES, pp. 135-176, NASA, Washington D.C., 1995.

936 Mlawer, E. J., Taubman, S. J., Brown, P. D., Iacono, M. J., and Clough, S. A.: Radiative transfer for inhomogeneous  
937 atmospheres: RRTM, a validated correlated-k model for the longwave, *J. Geophys. Res.*, 102, 16663-16682,  
938 <https://doi.org/10.1029/97JD00237>, 1997.

939 Molod, A., Takacs, L., Suarez, M., Bacmeister, J., Song, I.-S., and Eichman, A.: The GEOS-5 atmospheric general  
940 circulation model: Mean climate from MERRA to Fortuna, Technical Report Series on Global Modeling and  
941 Assimilations, Vol. 28, 124 pp, 2012.

942 Nakanishi, M., and Niino, H.: Development of an improved turbulence closure model for the atmospheric boundary  
943 layer, *J. Meteor. Soc. Japan*, 87, 895–912, <https://doi.org/10.2151/jmsj.87.895>, 2009.

944 Ogura, Y., and Cho, H.-R.: Diagnostic determination of cumulus cloud populations from observed large-scale  
945 variables, *J. Atmos. Sci.*, 30, 1276-1286, [https://doi.org/10.1175/1520-  
946 0469\(1973\)030<1276:DDOCCP>2.0.CO;2](https://doi.org/10.1175/1520-0469(1973)030<1276:DDOCCP>2.0.CO;2), 1973.

947 Olson, J.B., Kenyon, J.S., Angevine, W.M., Brown, J.M., Pagowski, M., and Suselj, K.: A description of the MYNN-  
948 EDMF scheme and the coupling to other components in WRF-ARW, NOAA Technical Memorandum OAR GSD,  
949 61, pp 37, 2019.

950 Platnick, S., King, M.D., Ackerman, S.A., Wenzel, W.P., Baum, B.A., Riedl, J.C., and Frey, R.A.: The MODIS cloud  
951 products: Algorithms and examples from Terra, *IEEE T. Geosci. Remote*, 41, 459-473,  
952 <https://doi.org/10.1109/TGRS.2002.808301>, 2003.

953 Qiao, F., and Liang, X-Z: Effects of cumulus parameterization closures on the simulations of summer precipitation  
954 over the United States coastal oceans, *J. Adv. Model. Earth Sy.*, 8, 764-785,  
955 <https://doi.org/10.1002/2015MS000621>, 2015.

956 Raymond, D.J.: Regulation of moist convection over the west Pacific warm pool, *J. Atmos. Sci.*, 52, 3945-3959,  
957 [https://doi.org/10.1175/1520-0469\(1995\)052<3945:ROMCOT>2.0.CO;2](https://doi.org/10.1175/1520-0469(1995)052<3945:ROMCOT>2.0.CO;2), 1995.

958 Schwarz, C.S.: Medium-range convection-allowing ensemble forecasts with a variable-resolution global model, *Mon.*  
959 *Weather Rev.*, 147, 2997-3023, <https://doi.org/10.1175/MWR-D-18-0452.1>, 2019.

960 Simpson, J., and Wiggert, V.: Models of precipitating cumulus towers, *Mon. Weather Rev.*, 97, 471-489,  
961 [https://doi.org/10.1175/1520-0493\(1969\)097<0471:MOPCT>2.3.CO;2](https://doi.org/10.1175/1520-0493(1969)097<0471:MOPCT>2.3.CO;2), 1969.

962 Skamarock, W.C., and Gassmann, A.: Conservative transport schemes for spherical geodesic grids: High-order flux  
963 operators for ODE-based time integration, *Mon. Weather Rev.*, 139, 2962-2975, [https://doi.org/10.1175/MWR-  
964 D-10-05056.1](https://doi.org/10.1175/MWR-D-10-05056.1), 2011.

965 Skamarock, W.C., Klemp, J.B., Duda, M.G., Fowler, L.D., Park, S.-H., and Ringler, T.D.: A multiscale nonhydrostatic  
966 atmospheric model using Centroidal Voronoi tessellations and C-grid staggering, *Mon. Weather Rev.*, 140, 3090-  
967 3105, <https://doi.org/10.1175/MWR-D-11-00215.1>, 2012.

968 Skamarock, W.C., and Coauthors: A description of the Advanced Research WRF version 3, NCAR Tech. Note  
969 NCAR/TN-475+STR, 113 pp, 2008.

970 Smagorinsky, J.: General circulation experiments with the primitive equations. I. The basic experiment, *Mon. Weather*  
971 *Rev.*, 91, 99-164, [https://doi.org/10.1175/1520-0493\(1963\)091<0099:GCEWTP>2.3.CO;2](https://doi.org/10.1175/1520-0493(1963)091<0099:GCEWTP>2.3.CO;2), 1963.

972 Stanfield, R.E., Dong, X., Xi, B., Del Genio, A.D., Minnis, P., Doelling, D., and Loeb, N.: Assessment of NASA  
973 GISS CMIP5 and Post-CMIP5 simulated clouds and TOA radiation budgets using satellite observations. Part II:  
974 TOA radiation budget and CREs, *J. Climate*, 28, 1842-1863, <https://doi.org/10.1175/JCLI-D-14-00249.1>, 2015.

975 Stephens, G.L., and Kummerow, C.D.: The remote sensing of clouds and precipitation from space: A review, *J. Atmos.*  
976 *Sci.*, 64, 3742-3765, <https://doi.org/10.1175/2006JAS2375.1>, 2007.

977 Stephens, G.L., Vane, D.G., Boain, R.J., Mace, G.G., Sassen, K., Wang, Z., Illingworth, A.J., O'Connor, E.J., Rossow,  
978 W.B., Durden, S.L., Miller, S.D., Austin, R.T., Benedetti, A., Mitrescu, C., and the CloudSat Science Team: The  
979 CloudSat mission and the A-Train: A new dimension and space-based observations of clouds and precipitation,  
980 *B. Am. Meteorol. Soc.*, 83, 1771-1790, <https://doi.org/10.1175/BAMS-83-12-1771>, 2002.

981 Storer, R.L., Griffin, B.M., Hoft, J., Weber, J.K., Raut, E., Larson, V.E., Wang, M., and Rasch, P.J.: Parameterizing  
982 deep convection using the assumed probability density function method, *Geosci. Model Dev.*, 8, 1-19,  
983 <https://doi.org/10.5194/gmd-8-1-2015>, 2015.

984 Suhas, E., and Zhang, Q.J.: Evaluation of trigger functions for convective parameterization schemes using  
985 observations, *J. Climate*, 27, 7647-7666, <https://doi.org/10.1175/JCLI-D-13-00718.1>, 2014.

986 Taylor, K.E., Stouffer, R.J., and Meehl, G.A.: An overview of CMIP5 and the experiment design, *B. Am. Meteorol.*  
987 *Soc.*, 93, 485-4398, <https://doi.org/10.1175/BAMS-D-11-00094.1>, 2012.

988 Thayer-Calder, K., Gettelman, A., Craig, C., Goldhaber, S., Bogenschutz, P.A., Chen, C.-C., Morrison, H., Höft, J.,  
989 Raut, E., Griffin, B.M., Weber, J.K., Larson, V.E., Wyant, M.C., M. Wang, Guo, Z., and Ghan, S.J.: A unified  
990 parameterization of clouds and turbulence using CLUBB and subcolumns in the Community Atmosphere Model,  
991 *Geosci. Model Dev.*, 8, 3801-3821, <https://doi.org/10.5194/gmd-8-3801-2015>, 2015.

992 Thompson, G., Field, P.R., Rasmussen, R.M., and Hall, W.D.: Explicit forecasts of winter precipitation using an  
993 improved bulk cloud microphysics scheme. Part II: Implementation of a new snow parameterization, *Mon.*  
994 *Weather Rev.*, 136, 5095-5115, <https://doi.org/10.1175/2008MWR2387.1>, 2008.

995 Thompson, G., Rasmussen, R.M., and Manning, K.: Explicit forecasts of winter precipitation using an improved bulk  
996 cloud microphysics scheme. Part I: Description and sensitivity analysis, *Mon. Weather Rev.*, 132, 519-542,  
997 [https://doi.org/10.1175/1520-0493\(2004\)132<0519:EFOWPU>2.0.CO;2](https://doi.org/10.1175/1520-0493(2004)132<0519:EFOWPU>2.0.CO;2), 2004.

998 Thompson, G., Tewari, M., Ikeda, K., Tessoroff, S., Weeks, C., Otkin, J., and Kong, F.: Explicitly-coupled cloud  
999 physics and radiation parameterizations and subsequent evaluation in WRF high-resolution convective forecasts,  
1000 *Atmos. Res.*, 168, 92-104, <https://doi.org/10.1016/j.atmosres.2015.09.005>, 2016.

1001 Tokioka, T., Yamazaki, K., Kotoh, A., and Ose, T.: The equatorial 30-60 day oscillation and the Arakawa-Schubert  
1002 penetrative cumulus parameterization, *J. Meteor. Soc. Japan*, 66, 883-900,  
1003 [https://doi.org/10.2151/jmsj1965.66.6\\_883](https://doi.org/10.2151/jmsj1965.66.6_883), 1988.

1004 Waliser, D.E., Li, J.-L., Woods, C.P., Austin, R.T., Bacmeister, J., Chern, J., Del Genio, A., Jiang, J.H., Juang, Z.,  
1005 Meng, H., Minnis, P., Platnick, S., Rossow, W.B., Stephens, G.L., Sun-Mack, S., Tao, W.-K., Tompkins, A.M.,

1006 Vane, D.G., Walker, C., and Wu, D.: Cloud ice: A climate model challenge with signs and expectations of  
1007 progress, *J. Geophys. Res.*, 114, D00A21, <https://doi.org/10.1029/2008JD010015>, 2009.

1008 Wicker, L.J., and W.C. Skamarock: Time-splitting methods for elastic models using forward time schemes, *Mon.*  
1009 *Weather Rev.*, 130, 2088-2097, [https://doi.org/10.1175/1520-0493\(2002\)130<2088:TSMFEM>2.0.CO;2](https://doi.org/10.1175/1520-0493(2002)130<2088:TSMFEM>2.0.CO;2), 2002.

1010 Wielicki, B.A., Barkstrom, B.R., Harrison, E.F., Lee III, R.B., Smith, G.L., and Cooper, J.E.: Clouds and the Earth's  
1011 Radiation Energy System (CERES): An Earth Observing System experiment, *B. Am. Meteorol. Soc.*, 77, 853-  
1012 868, [https://doi.org/10.1175/1520-0477\(1996\)077<0853:CATERE>2.0.CO;2](https://doi.org/10.1175/1520-0477(1996)077<0853:CATERE>2.0.CO;2), 1996.

1013 Wong, M., and Skamarock, W.C.: Spectral characteristics of convective-scale precipitation observations and forecasts,  
1014 *Mon. Weather Rev.*, 144, 4183-4195, <https://doi.org/10.1175/MWR-D-16-0183.1>, 2016.

1015 Xu, K.-M. and Krueger, S.K.: Evaluation of cloudiness parameterizations using a cumulus ensemble model, *Mon.*  
1016 *Weather Rev.*, 119, 342-367, [https://doi.org/10.1175/1520-0493\(1991\)119<0342:EOCPUA>2.0.CO;2](https://doi.org/10.1175/1520-0493(1991)119<0342:EOCPUA>2.0.CO;2), 1991.

1017 Xu, K.-M., and Randall, D. A.: A semi-empirical cloudiness parameterization for use in climate models, *J. Atmos.*  
1018 *Sci.*, 53, 3084–3102, [https://doi.org/10.1175/1520-0469\(1996\)053<3084:ASCPFU>2.0.CO;2](https://doi.org/10.1175/1520-0469(1996)053<3084:ASCPFU>2.0.CO;2), 1996.

1019 Zheng, Y., Alapaty, K., Herwehe, J. A., Del Genio, A.D., and Niyogi, D.: Improving high-resolution weather forecasts  
1020 using the Weather Research and Forecasting (WRF) model with an updated Kain-Fritsch scheme, *Mon. Weather*  
1021 *Rev.*, 144, 833-860, <https://doi.org/10.1175/MWR-D-15-0005.1>, 2016.